



# รายงานวิจัยฉบับสมบูรณ์

โครงการ ไขความลับทางวิวัฒนาการของการปลดปล่อยก๊าซ จาก

> กาแล็กซี่ด้วยข้อมูลจากการสำรวจผ่านอุปกรณ์ ไฮเปอร์สุพริ่มแคมของหอดูดาวซูบารุ

โดย ผู้ช่วยศาสตราจารย์ ดร. สุรพงษ์ อยู่มา

เดือน ปี ที่เสร็จโครงการ พฤษภาคม พ.ศ. 2563

# รายงานวิจัยฉบับสมบูรณ์

โครงการ ไขความลับทางวิวัฒนาการของการปลดปล่อยก๊าซ จาก

> กาแล็กซี่ด้วยข้อมูลจากการสำรวจผ่านอุปกรณ์ ไฮเปอร์สุพรีมแคมของหอดูดาวซูบารุ

โดย ผู้ช่วยศาสตราจารย์ ดร. สุรพงษ์ อยู่มา ภาควิชาฟิสิกส์ คณะวิทยาศาสตร์ มหาวิทยาลัยมหิดล

สนับสนุนโดยสำนักงานคณะกรรมการการอุดมศึกษาและสำนักงานกองทุนสนับสนุนการวิจัย

(ความเห็นในรายงานนี้เป็นของผู้วิจัย สกอ. และ สกว. ไม่จำเป็นต้องเห็นด้วยเสมอไป)

**Abstract** 

Project Code: MRG6180279

Project Title: Unveiling the Evolution of Galactic-scale Outflows with the

Subaru/Hyper Suprime-Cam Survey

Investigator: Asst. Prof. Dr. Suraphong Yuma

Department of Physics, Faculty of Science, Mahidol University

E-mail Address: suraphong.yum@mahidol.ac.th

Project Period: 2 years (July 2018 - June 2020)

We conducted a systematic search for galaxies with [OII]λ3727, [OIII]λ5007, and H $\alpha\lambda$ 6563 emission lines extended over at least 30 kpc (9x10<sup>17</sup> km) at z=0.1-1.5 covering the past 9 billion years of the universe. These extended emission-line galaxies are thought to be in the middle of gas outflow process on a galactic scale large enough to prevent star forming activity in the galaxies. We found 430 galaxies at z=0.40-1.46 based on our new selection method introduced in the previous TRF project (MRG5980153). This technique can securely identify galaxies with the extended emission line measured down to 1.2x10<sup>-18</sup> erg/s/cm<sup>2</sup>/kpc<sup>2</sup>. We further studied 4 [OIII] blobs at z=0.83 in details by using the spectroscopic data observed with the Subaru/FOCAS and Keck/MOSFIRE instruments. One of the [OIII] blobs, which we called a giant green pea, shows an extension of the [OIII] emission with the high [OIII]/[OII] ratio of 5-10 over 14 kpc. It suggests the high ionization parameter comparable with a compact green pea at z=0.3. This spatially extended [OIII] emission is likely originated from the outflowing gas produced by the intense star formation in the density bounded ionization state.

The results obtained during this TRF project are published in The Astrophysical Journal (Yuma et al. 2019, ApJ, 882, 17, 1-16; Q1 & IF=5.580).

**Keywords:** galaxies: evolution, galaxies: formation, galaxies: high-redshift

รหัสโครงการ: MRG6180279

ชื่อโครงการ: ไขความลับทางวิวัฒนาการของการปลดปล่อยก๊าซจากกาแล็กซี่ด้วยข้อมูล จากการสำรวจผ่านอุปกรณ์ไฮเปอร์สุพรีมแคมของหอดูดาวซูบารุ

ชื่อนักวิจัย: ผศ. ดร. สุรพงษ์ อยู่มา ภาควิชาฟิสิกส์ คณะวิทยาศาสตร์ มหาวิทยาลัยมหิดล

E-mail Address: suraphong.yum@mahidol.ac.th

# ระยะเวลาโครงการ: 2 ปี (กรกฎาคม 2561 – มิถุหายห 2563)

กาแล็กซี่ คือ ระบบ ที่ประกอบด้วยดาวฤกษ์นับล้านๆดวง และกลุ่มก๊าซชนิดต่างๆ มากมาย เช่น กาแล็กซี่ทางช้างเผือกซึ่งเป็นที่อยู่ของระบบสุริยะของเรา จักรวาลประกอบไป ด้วยกาแล็กซี่หลายชนิดทั้งที่เป็นรูปกังหันที่กำลังสร้างดาวฤกษ์ใหม่ๆ และแบบรีที่ไม่มีการสร้าง ดาวใหม่แล้ว งานวิจัยชิ้นนี้ เป็นการสำรวจหากาแล็กซี่แบบกังหัน ที่กำลังจะเปลี่ยนไปเป็นกา โดยการปลดปล่อยก๊าซออกจากกาแล็กซี่ซึ่งเป็นเหตุให้การสร้างดาวหยุดลง แล็กซี่แบบรี กระบวนการนี้นับเป็นกระบวนการที่สำคัญอย่างมาก ในการทำความเข้าใจการเกิดและ วิวัฒนาการของกาแล็กซี่ในจักรวาล เราได้ใช้วิธีใหม่ในการค้นหากาแล็กซี่ที่อยู่ในกระบวนการ หยุดสร้างดาวอย่างมีระบบ ซึ่งได้ศึกษาไว้ในโครงการวิจัยที่แล้ว (MRG5980153) โดยการใช้ ระเบียบขั้นตอนทางคอมพิวเตอร์ เพื่อให้สามารถคัดกรองกาแล็กซี่ได้ครั้งละหลายพันระบบ นั่น คือ เราจะสามารถคำนวณได้ว่า มีกาแล็กซี่ที่อยู่ในกระบวนการนี้เป็นปริมาณเท่าไรในช่วงเวลา หนึ่งๆ ของจักรวาล เราค้นพบ 430 กาแล็กซี่ที่เรดชิพ 0.40-1.46 งกาแล็กซี่นี้บางส่วนได้ถูก สังเกตการณ์ด้วยกล้องโทรทรรศน์ซูบารุและเคค หนึ่งในนั้นแสดงการปลดปล่อยก๊าซออกซิเจน ออกมาในบริเวณกว้าง และมีค่าไอออไนเซชันพารามิเตอร์สูงกว่าปกติมาก เราเรียกว่า Giant green pea ซึ่งคาดว่า น่าจะเป็นผลมาจาก การปลดปล่อยก๊าซในกรณี density bounded ionization

ผลที่ได้จากโครงการวิจัยนี้ ได้ถูกตีพิมพ์เผยแพร่ ในวารสาร Astrophysical Journal (Yuma et al. 2019, ApJ, 882, 17, 1-16; Q1 & IF=5.580)

คำหลัก: วิวัฒนาการของกาแล็กซี่, การเกิดของกาแล็กซี่, กาแล็กซี่ที่อยู่ไกล

# **Executive Summary**

# Unveiling the Evolution of Galactic-scale Outflows with the Subaru/Hyper Suprime-Came Survey

by Suraphong Yuma (Department of Physis, Faculty of Science, Mahidol University)

### 1 Introduction to research problem and its significance

A galaxy is one of the complicated astronomical objects containing billions of stars like the Sun. Galaxies are historically divided into two main types according to their appearances: a spiral/disk galaxy, and an elliptical galaxy. This is known as "Hubble Sequence." The spiral galaxy mainly consists of young stars with multiple spiral arms where the star formation occurs. Large amounts of gas and dust, which are crucial ingredients in star formation process, reside in this type of galaxy and turn into new stars at star formation rate (SFR) typically in the order of a few to hundreds of solar masses per year. On the other hand, an elliptical galaxy is featureless, contains mostly old stars, and rarely forms new stars. Astronomers have been trying to figure out how these galaxies evolve along the timeline of the universe. However, lifetime of the galaxies is too long (in the order of more than hundreds billion years) that we cannot specifically study the evolution of one particular galaxy within our lifetime. What we can do is to study as many galaxies as possible at various epochs of the universe to gain insight into the galaxy populations at each epoch and eventually the entire process of galaxy evolution.

Many studies on the number density and stellar mass of galaxies up to z~1 suggest that star formation in spiral galaxies needs to be halted causing them to migrate into the red sequence (e.g., McIntosh et al. 2005; Bundy et al. 2006; Faber et al. 2007). The mechanism that prevents the galaxy from forming new stars is called "the quenching process." After this process, the galaxy would not form any new stars including the massive ones that emit the rest-frame UV continuum. At the age of >10 Myr, the most massive stars in the galaxy die and become red supergiant stars, causing the UV light to decline and the near-infrared light to increase. The rest-frame UV continuum continues to decrease when the galaxy becomes older as the relatively less massive stars continuously die, leaving only long-lived low-mass stars with dominated rest-frame optical continuum in the galaxy. Consequently, the galaxy becomes redder and moves to the red sequence. The quenching process is an unarguably crucial process in studying galaxy evolution.

In 2013, we conducted the first systematic search for galaxies with spatially extended oxygen emission and found 12 galaxies, dubbed "[OII] blobs," at z~1.2 in the Subaru XMM Deep Survey (SXDS) presenting large (>30kpc) extended [OII] emission (Yuma et al. 2013). These extended oxygen nebulae beyond the stellar component are thought to be the hot metal-rich gas outflowing from galaxies rather than pristine gas inflowing from metal-poor intergalactic space. Searching for galaxies with extended oxygen emission provides us a systematic sample of galaxies showing hot metal-rich large-scale outflow both with and without an AGN. Although extended oxygen emission is already seen in some AGNs, this was the first time for a systematic sample of large-scale outflows in non-AGN galaxies.

Our method is very successful in systematically selecting galaxies with large-scale outflows using only the imaging data. So, in our previous TRF proposal (MRG5980153) we extended the search toward lower and higher redshifts in attempt to understand the big picture of the evolution of the gas outflow, AGN/stellar feedback, and eventually the galaxy. Parts of the results are already published in the Astrophysical journal with the impact factor of 5.533 in 2016 (Yuma et al. 2017). Covering the past 9 billion years of the universe, we found 77 galaxies at z = 0.40-1.46 with [OII]3727, [OIII]5007, and Hα6563 emission lines spatially extended over 30kpc. We call them [OII], [OIII], and  $H\alpha$  blobs, respectively. We could confirm that the stellar masses of our blobs are statistically larger than those of normal star forming galaxies discovered at the same epoch. We also found the blobs with extended emission lines only at the two highest epochs of our previous survey (z=1.19 and z=1.46), while there are only upper limits at other epochs. It is fair to state that the evolution of the galaxies with gas outflow in the scale large enough to halt star formation activity is still unknown for most of the time. This is because of the limited field of views of our previous survey data at lower redshifts. At the same angular size of the survey area, the physical area on the sky and the subsequent survey volume become smaller at lower redshifts. In order to gain full insight into galaxy evolution, we need perform a new search of the outflowing galaxies with a significantly larger sky survey.

### 2 Objectives

- 2.1 To fill in the missing pieces in studying the evolution of large-scale outflows over the past 8 billion years (at z<1.0) that were left incomplete in our previous TRF project.
- 2.2 To enhance the sample of blobs at z>1.0. This will significantly improve the statistics of our studies, as the new survey covers a remarkably larger area than before.
- 2.3 To understand the evolution of AGN/stellar feedback and subsequent quenching process that turns star-forming galaxies into passively evolving elliptical galaxies.
- 2.4 To request telescope time for spectroscopic follow-up observations, which could lead to understanding of the physical mechanisms behind galactic-scale outflows of gas.

### 3 Methodology

3.1 Constructing the emission-line images

In order to examine if a galaxy at the targeted redshift exhibits the extended emission line or not, we need to carefully make an emission-line image that shows only the emission-line component. The images that contain only the flux from emission lines can be constructed by subtracting the narrowband images with the broadband images at approximately the same wavelength. The narrowband image contains the light from both the desired emission line and stellar continuum of the galaxy. Hence, we need to subtract the interpolated continuum from the narrowband images to make the emission-line images. The narrowband and broadband images at the corresponding wavelength are often obtained with different quality. Before we construct the emission-line images out of the original narrowband and broadband ones, we need to perform the coordinate registration and normalize the seeing size of the point spread function to synchronize the coordinates of all objects

observed in those two images and to match the objects' sizes so that the point sources or stars show zero flux in the resulting emission-line images.

3.2 Crossmatching [OII], [OIII], and Ha emitters at z=0-1.5

We will first make a photometric catalog that contains coordinates and magnitudes of objects detected in the emission-line images by using Source Extractor program. The catalog will then be crossmatched with the catalogs of star forming galaxies with strong emission lines at z=0-1.5 by Hayashi et al. (2017). The galaxy catalog by Hayashi et al. (2017) contain unprecedentedly large samples of 63,000 galaxies with strong [OII], [OIII], and Ha emission lines.

3.3 Isolating [OII], [OIII], and Ha blobs with galactic-scale outflow from normal galaxies

We will select only those showing the extended features of the emission line by creating the equivalent width (EW) map of each galaxy. We developed a new selection method to automatically isolate the blobs with genuinely extended emission line by using the EW map. At the end of this step, we expect more than 4000 galaxies to be selected from z=0.25 to z=1.7 covering almost the past 10 billion years of the universe.

3.4 Determining the stellar populations of all blobs by SED fitting

After we obtain complete sample of blobs with large-scale outflow from the previous step, we will determine their physical properties by using the method called SED fitting. The photometry of blobs can be plotted as a function of wavelength; it is called the spectral energy distribution (SED). The SED of each blob will be compared with the modeled SEDs that are constructed by varying the stellar mass, age, dust extinction, and SFR. We will investigate and discuss the correlation between the physical properties of blobs and their extension of emission lines. The evolution of these properties of blobs can also be discussed. Furthermore, it is also interesting to figure out any physical difference between blobs and normal galaxies at the same epoch of the universe.

3.5 Examining the physical mechanism responsible for large-scale outflows.

The HSC survey will provide huge amount of good galaxy candidates with large-scale outflow relating to strong feedback for the follow-up observations in optical, infrared, and millimetre/submillimeter wavelengths. We will request for telescope time and conduct the follow-up observations to further examine the energy sources (AGN or stellar feedback) and the details of physical process in producing the large-scale outflow. Roles of AGN/stellar feedback on the galactic outflow and star formation quenching will be revealed with great statistical improvement.

3.6 Investigating number densities of blobs with large-scale outflow at each epoch, their evolution with time, and relation with the cosmic star formation history of the universe. As a systematic search, we are able to determine the number densities of blobs at each specific epoch of the universe and eventually discuss their evolution and subsequent quenching process from z=1.7 to z=0. With these HSC data, we will be able to provide insight into the evolution of blobs at redshifts below z=1.0 where only the upper limits are provided with the current data. The outflow evolution can then be related with the decline of cosmic star formation density toward the present-say universe to examine the role of large-scale outflow in stopping the star forming activity of galaxies and the universe.

### 4 Schedule of the entire project

Schedule	Timeline
Constructing the emission-line image	The first 3 months
Crossmatching [OII], [OIII], and Ha emitters at z=0-1.5	Within the 4 <sup>th</sup> month of the first year
Isolating [OII], [OIII], and Ha blobs with galactic-scale	5 <sup>th</sup> -7 <sup>th</sup> months of the first year
outflow from normal galaxies	
Determining the stellar populations of all blobs by SED	8 <sup>th</sup> -9 <sup>th</sup> months of the first year
fitting	
Examining the physical mechanism responsible for	The rest of the first year + the first 3
large-scale outflows.	months of the 2 <sup>nd</sup> year
Investigating number densities of blobs with large-scale	3 <sup>rd</sup> -6 <sup>th</sup> months of the 2 <sup>nd</sup> year
outflow at each epoch, their evolution with time, and	
relation with the cosmic star formation history of the	
universe	
Preparing and submitting at least one paper to the	To the end of the 2 <sup>nd</sup> year
Astrophysical Journal	

# **5** Expected paper to be submitted in an international journal

Expected title: Evolution of large-scale outflow by Subaru/HSC strategic survey

Journal: Astrophysical Journal (ApJ)

Impact factor: 5.533 (2016)

# 6 Budget details (All entries are in Thai Baht.)

	1 <sup>st</sup> year	2 <sup>nd</sup> year	Total
1. Honorarium			
PI - :Suraphong Yuma	156,000	156,000	312,000
2. Materials			
- Computer materials for an upgrade	50,000	0	50,000
- Office materials	4000	24,000	28,000
3. Expenses			
- Page charge for publication	0	50,000	50,000
- Image checking fee (data processing and analysis)	50,000	20,000	80,000
- Domestic travel expense (for research and			
presentation at the conference)	30,000	40,000	60,000
- Domestic travel expenses for TRF activities			
- Report preparation	5,000	5,000	10,000
	5,000	5,000	10,000
Total budget	300,000	300,000	600,000

### Research content

### 1. Introduction to research problem and its significance

A galaxy is one of the complicated astronomical objects containing billions of stars like the Sun. Galaxies are historically divided into two main types according to their appearances: a spiral/disk galaxy, and an elliptical galaxy. This is known as "Hubble Sequence." The spiral galaxy mainly consists of young stars with multiple spiral arms where the star formation occurs. Large amounts of gas and dust, which are crucial ingredients in star formation process, reside in this type of galaxy and turn into new stars at star formation rate (SFR) typically in the order of a few to hundreds of solar masses per year. On the other hand, an elliptical galaxy is featureless, contains mostly old stars, and rarely forms new stars. Astronomers have been trying to figure out how these galaxies evolve along the timeline of the universe. However, lifetime of the galaxies is too long (in the order of more than hundreds billion years) that we cannot specifically study the evolution of one particular galaxy within our lifetime. What we can do is to study as many galaxies as possible at various epochs of the universe to gain insight into the galaxy populations at each epoch and eventually the entire process of galaxy evolution.

Many studies on the number density and stellar mass of galaxies up to z~1 suggest that star formation in spiral galaxies needs to be halted causing them to migrate into the red sequence (e.g., McIntosh et al. 2005; Bundy et al. 2006; Faber et al. 2007). The mechanism that prevents the galaxy from forming new stars is called "the quenching process." After this process, the galaxy would not form any new stars including the massive ones that emit the rest-frame UV continuum. At the age of >10 Myr, the most massive stars in the galaxy die and become red supergiant stars, causing the UV light to decline and the near-infrared light to increase. The rest-frame UV continuum continues to decrease when the galaxy becomes older as the relatively less massive stars continuously die, leaving only long-lived low-mass stars with dominated rest-frame optical continuum in the galaxy. Consequently, the galaxy becomes redder and moves to the red sequence. The quenching process is an unarguably crucial process in studying galaxy evolution.

In 2013, we conducted the first systematic search for galaxies with spatially extended oxygen emission and found 12 galaxies, dubbed "[OII] blobs," at z~1.2 in the Subaru XMM Deep Survey (SXDS) presenting large (>30kpc) extended [OII] emission (Yuma et al. 2013). These extended oxygen nebulae beyond the stellar component are thought to be the hot metal-rich gas outflowing from galaxies rather than pristine gas inflowing from metal-poor intergalactic space. Searching for galaxies with extended oxygen emission provides us a systematic sample of galaxies showing hot metal-rich large-scale outflow both with and without an AGN. Although extended oxygen emission is already seen in some AGNs, this was the first time for a systematic sample of large-scale outflows in non-AGN galaxies.

Our method is very successful in systematically selecting galaxies with large-scale outflows using only the imaging data. So, in our previous TRF proposal (MRG5980153) we extended the search toward lower and higher redshifts in attempt to understand the big picture of the evolution of the gas outflow, AGN/stellar feedback, and eventually the galaxy. Parts of the results are already

published in the Astrophysical journal with the impact factor of 5.533 in 2016 (Yuma et al. 2017). Covering the past 9 billion years of the universe, we found 77 galaxies at z=0.40-1.46 with [OII]3727, [OIII]5007, and H $\alpha$ 6563 emission lines spatially extended over 30kpc. We call them [OII], [OIII], and H $\alpha$  blobs, respectively. We could confirm that the stellar masses of our blobs are statistically larger than those of normal star forming galaxies discovered at the same epoch. We also found the blobs with extended emission lines only at the two highest epochs of our previous survey (z=1.19 and z=1.46), while there are only upper limits at other epochs. It is fair to state that the evolution of the galaxies with gas outflow in the scale large enough to halt star formation activity is still unknown for most of the time. This is because of the limited field of views of our previous survey data at lower redshifts. At the same angular size of the survey area, the physical area on the sky and the subsequent survey volume become smaller at lower redshifts. In order to gain full insight into galaxy evolution, we need perform a new search of the outflowing galaxies with a significantly larger sky survey.

### 2. Objectives

- a. To fill in the missing pieces in studying the evolution of large-scale outflows over the past 8 billion years (at z<1.0)</li>
- b. To enhance the sample of blobs at z>1.0.
- c. To understand the evolution of AGN/stellar feedback and subsequent quenching process that turns star-forming galaxies into passively evolving elliptical galaxies.
- d. To request telescope time for spectroscopic follow-up observations, which could lead to understanding of the physical mechanisms behind galactic-scale outflows of gas.

# 3. Methodology

### a. Constructing the emission-line images

In order to examine if a galaxy at the targeted redshift exhibits the extended emission line or not, we need to carefully make an emission-line image that shows only the emission-line component. The images that contain only the flux from emission lines can be constructed by subtracting the narrowband images with the broadband images at approximately the same wavelength. The narrowband image contains the light from both the desired emission line and stellar continuum of the galaxy. Hence, we need to subtract the interpolated continuum from the narrowband images to make the emission-line images. The narrowband and broadband images at the corresponding wavelength are often obtained with different quality. Before we construct the emission-line images out of the original narrowband and broadband ones, we performed the coordinate registration and normalize the seeing size of the point spread function to synchronize the coordinates of all objects observed in those two images and to match the objects' sizes so that the point sources or stars show zero flux in the resulting emission-line images.

### b. Crossmatching [OII], [OIII], and Ha emitters at z=0-1.5

We made a photometric catalog that contains coordinates and magnitudes of objects detected in the emission-line images by using Source Extractor program. The catalog is crossmatched with the catalogs of star forming galaxies with strong emission lines at z=0-1.5 by Hayashi et al. (2017), which contain unprecedentedly large samples of 63,000 galaxies with strong [OII], [OIII], and Ha emission lines.

# c. Isolating [OII], [OIII], and Ha blobs with galactic-scale outflow from normal galaxies

We then selected only those showing the extended features of the emission line by creating the equivalent width (EW) map of each galaxy. We developed a new selection method to automatically isolate the blobs with genuinely extended emission line by using the EW map.

### d. Determining the stellar populations of all blobs by SED fitting

After we obtained the complete sample of blobs with large-scale outflow from the previous step, we determined their physical properties by using the method called SED fitting. The photometry of blobs is plotted as a function of wavelength; it is called the spectral energy distribution (SED). The SED of each blob was compared with the modeled SEDs that are constructed by varying the stellar mass, age, dust extinction, and SFR.

### e. Examining the physical mechanism responsible for large-scale outflows.

The HSC survey provides the huge amounts of good galaxy candidates with large-scale outflow relating to strong feedback for the follow-up observations in optical, infrared, and millimetre/submillimeter wavelengths. We wrote three proposals with collaboration with The university of Tokyo, UC Santa Babara, and University of Melbourne requesting for telescope times to further examine the energy sources (AGN or stellar feedback) and the details of physical process in producing the large-scale outflow. Roles of AGN/stellar feedback on the galactic outflow and star formation quenching will be revealed with great statistical improvement.

The spectroscopic follow-up observations of the blob sample are conducted with various telescopes such as Subaru, Keck, or Anglo-Australian telescope. The primary objective of the follow-up is to confirm the redshift of the sample. This step is crucial in eliminating the low-redshift contamination that might cause an overestimation in number densities of blobs at each epoch. Another objective is to study the physical mechanism behind the large-scale outflow that results in the spatially extended emission.

## 4. Results

(Note that the results are already published in The Astrophysical Journal)

### a. Ha, [OII], and [OIII] blobs at z=0.4-1.5

I constructed the emission-line images using only the data from the ultra-deep field, which is the smallest but deepest field of the HSC survey. After crossmatching the photometric catalog with the galaxies with the strong emission lines from Hayashi et al. (2018), the galaxies with spatially extended emission have been successfully obtained. Figure 1 shows an example of the preliminary results on the blob selection in the UD-SXDS and UD-COSMOS fields, which cover about 1.43 and 1.47 square degrees, respectively. The FOV of the UD-SDSS field is insignificantly greater than that of the previous SXDS survey I studied in the previous paper (Yuma et al. 2017), which covered about 1.3 square degrees. Although the survey volumes do not change, we obtain larger sample of blobs candidates with this current project as summarized in Table 1. It is clearly seen from the table that the numbers of blob candidates in the current HSC survey increase remarkably from the previous Suprime-Cam survey; i.e., from 77 blobs to 430 blobs. With this huge amount of sample, we will be able to have a better constraint on the evolution of number densities of galaxies with extended emission across various epochs of the universe. Examples of the newly selected blobs are shown in Figure 2. The extended emission is clearly seen in the figure.

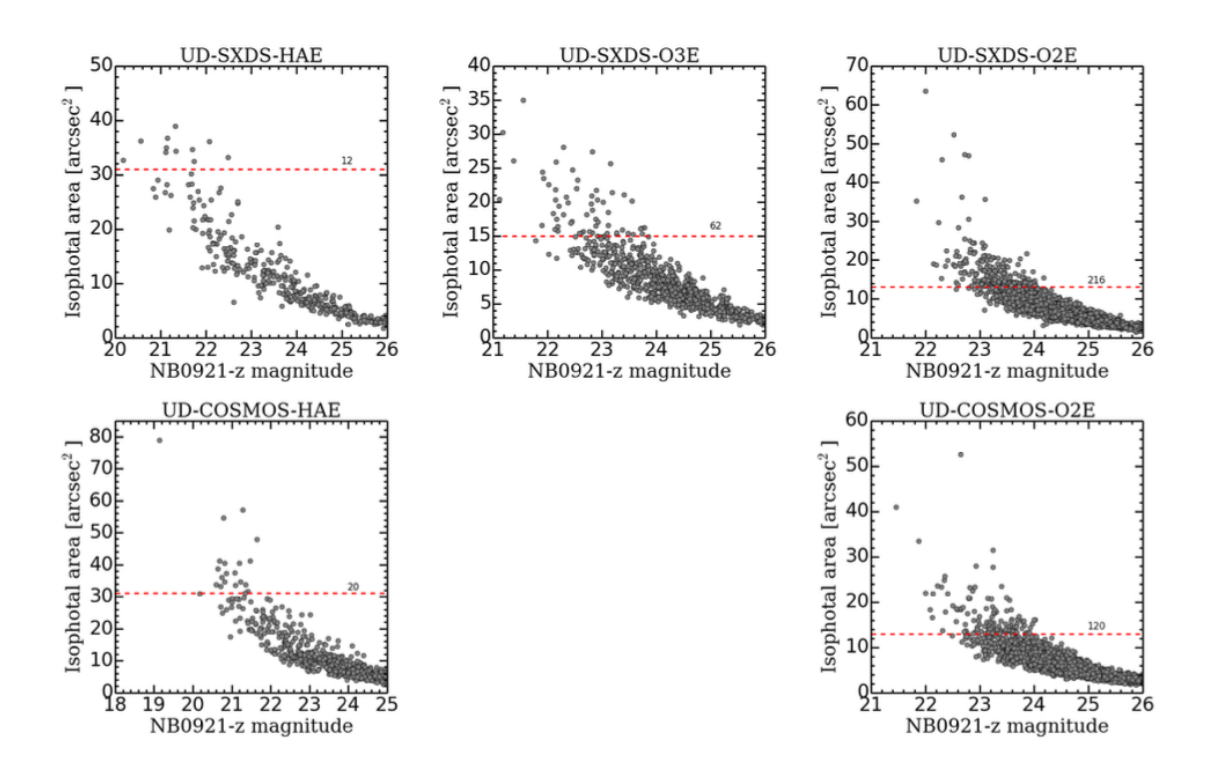


Figure 1. Magnitudes versus isophotal area of the galaxies with strong emission lines at various redshifts. H $\alpha$ , [OIII], and [OII] emitters at z = 0.40, z = 0.83, and z = 1.46 are shown in the left, middle, and right panels, respectively.

Table 1: Numbers of blob candidates found in UD-SXDS and UD-COSMOS fields in comparison with our previous SXDS survey

Redshift	Emission Line	Numbers of Blob Candidates		
		$\mathrm{SXDS}^a$	$\mathrm{UD}\text{-}\mathrm{SXDS}^b$	$\mathrm{UD\text{-}COSMOS}^b$
0.40	$H\alpha\lambda6563$	6	12	20
0.83	$[O III]\lambda 5007$	13	62	_
1.46	$[O II]\lambda 3727$	43	216	120

<sup>&</sup>lt;sup>a</sup> The number of blobs obtained from the previous SXDS survey with Subaru/Suprime-Cam (Yuma et al. 2017).
<sup>b</sup> The number of blob candidates found in this project with Subaru/HSC survey.

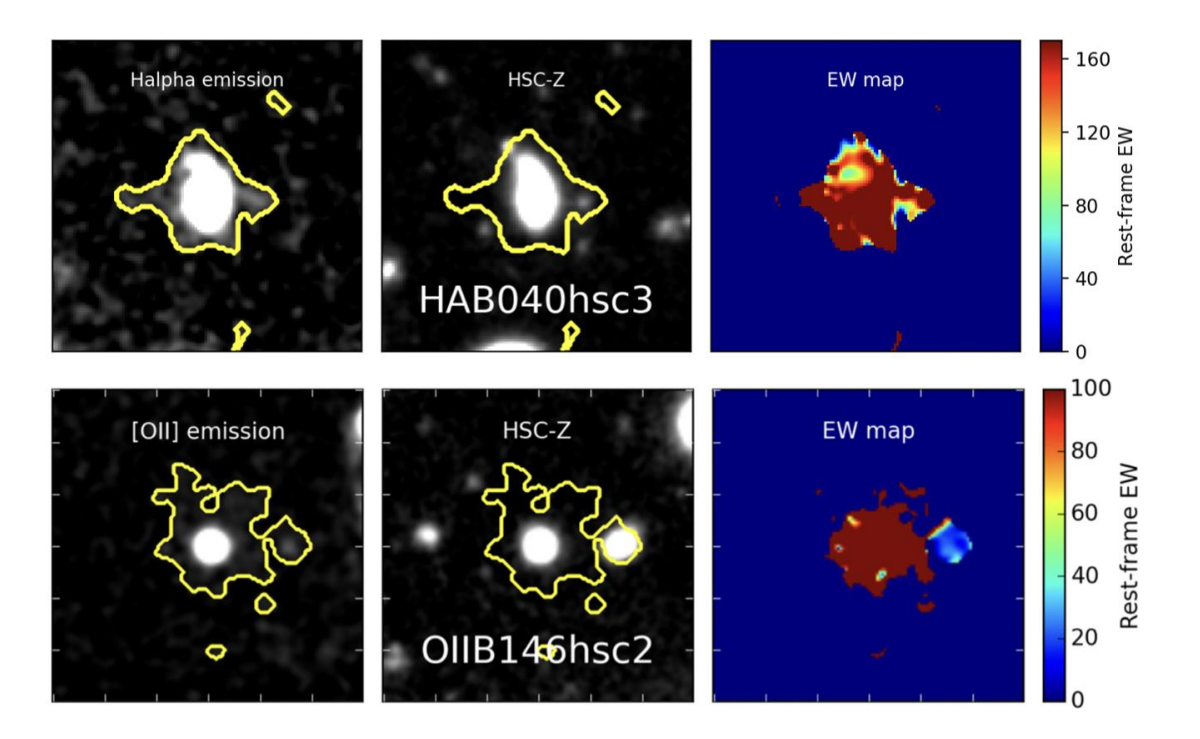


Figure 2: Emission-line, continuum, and EW map of blob examples at z=0.40 (top) and z=1.46 (bottom).

### b. Spectroscopic follow-up observations

My collaborators and I conducted the optical spectroscopic follow-up observations with Subaru/Faint Object Camera and Spectrograph (FOCAS; Kashikawa et al. 2002) on October 21—22, 2014 and December 2—4, 2015 (S14B-130 and S15B-059; PI: S. Yuma). Details about the Subaru/FOCAS spectroscopic observations are described in Yuma et al. (2017). Briefly speaking, we performed the observations in the multi-object spectroscopy (MOS) mode with the VPH450 grating and the VPH850 grating with the SO58 order-cut filter. The gratings cover 3800—5250 Å with a dispersion of 0.37 Å/pixel and 5800—10500 Å with 1.17 Å/pixel, respectively. We adopted the slit width of 0. 8 providing the spectral resolutions of 1700 and 750 for VPH450 and VPH850+SO58, respectively. Near-infrared (NIR) observation was conducted only for OIIIB-1 with Multi-Object Spectrometer For Infrared Exploration (MOSFIRE; McLean et al. 2012) attached on Keck I telescope. OIIIB-1 was observed as a filler target with the Y-band filter on January 3 — 4, 2014 (S15B-075; PI: M. Ouchi). The main objective of the MOSFIRE proposal is to confirm the Lyman alpha emitters at

 $z\sim5.7$ . The spectral resolution is 3388 with the standard 0.7" slit width. The total exposure time is 4.45 hours with seeing size of  $\sim0.7$  arcseconds.

Furthermore, we also performed the spectroscopic follow-up with AAOmega spectrograph attached on the Anglo-Australian Telescope in Australia. Twenty blob candidates are observed with the fiber in both blue and red arms covering the observed wavelengths of 3700—9500 Å. These AAT/AAOmega data are under the process of data reduction.

### c. Redshift confirmation

The Subaru/FOCAS spectra of 4 [OIII] blobs at z~0.63-0.83 are illustrated in Figure 3 at the observed wavelengths of the [OII] $\lambda$ 3727, H $\beta$  $\lambda$ 4861, and [OIII] $\lambda$  $\lambda$ 4959, 5007 emission lines. In each plot, we show the two-dimensional spectral image in the top panel and the one-dimensional spectrum in the bottom one. All the lines for a given blob are plotted with the same flux scale to provide the idea of the strength of the emission lines as compared to one another. The top row of Figure 3 shows that the stellar continuum is significantly detected in OIIIB-1. The excessive extension of the emission lines beyond the stellar components is clearly seen in the 2D spectral image. We fit the [OII], H $\beta$ , and [OIII] emission lines with a single Gaussian profile and adopt the center of the Gaussian profile that is best fitted to the [O iii] $\lambda$ 5007 emission line as the spectroscopic redshift for each [OIII] blob.

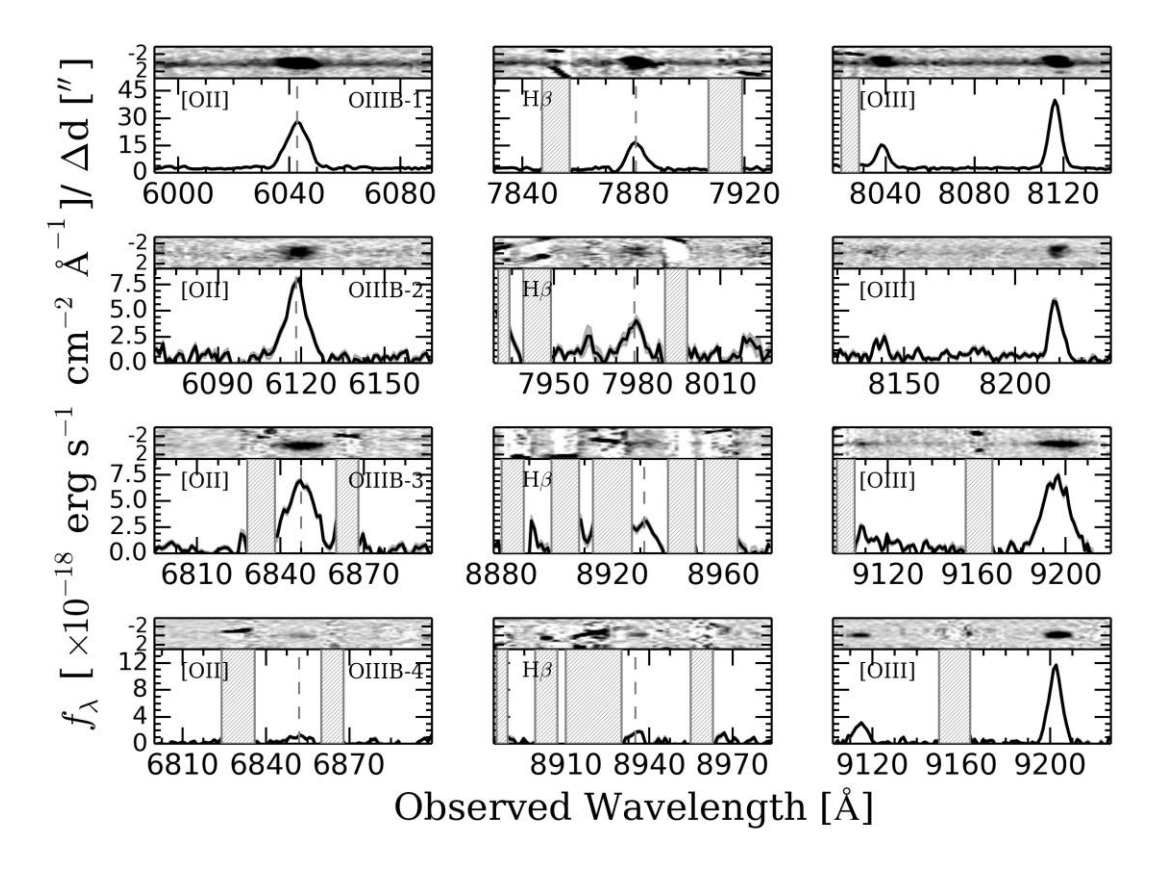


Figure 3: Subaru/FOCAS spectra of OIIIB-1, OIIIB-2, OIIIB-3, and OIIIB-4 from the top to the bottom panels, respectively. The left, middle, and right columns show the [OII],  $H\beta$ , and [OIII] emission lines of each object, respectively.

### d. Outflow signature

The galaxies with spatially extended emission lines like [OIII] blobs are thought to be in an ongoing process of the large-scale outflow. The gas outflow is already confirmed in [OII] blobs at z  $\sim 1.2$  with Subaru/FOCAS, VLT/VIMOS, and Magellan/LDSS spectra of the [OII] blobs at z  $\sim 1.2$  (Yuma et al. 2013; Harikane et al. 2014); however, this is the first time to confirm if the [OIII] blobs are in the middle of the outflow process. The blueshifted interstellar absorption lines are one of the most common methods that are used to study the outflow process of the galaxies. Unfortunately, the spectra of three out of four blobs in the VPH450 grating, in which we expect to detect the absorption lines, have too low S/N ratios. We only detect the absorption lines in the OIIIB-1 spectrum. Figure 4 shows the blueshifted Fe II $\lambda$ 2600 absorption, Fe II\* $\lambda$ 2626 fine-structure emission, and Mg II $\lambda$ 2804 absorption lines. They are all blueshifted from the systemic redshift, indicating the gas outflow from the galaxy. We fit the blueshifted absorption and emission lines with a single Gaussian profile. The velocity offsets of the Fe II, Fe II\*, and Mg II lines are  $-160 \text{ kms}^{-1}$ ,  $-200 \text{ kms}^{-1}$ , and  $-270 \text{ km s}^{-1}$ , respectively.

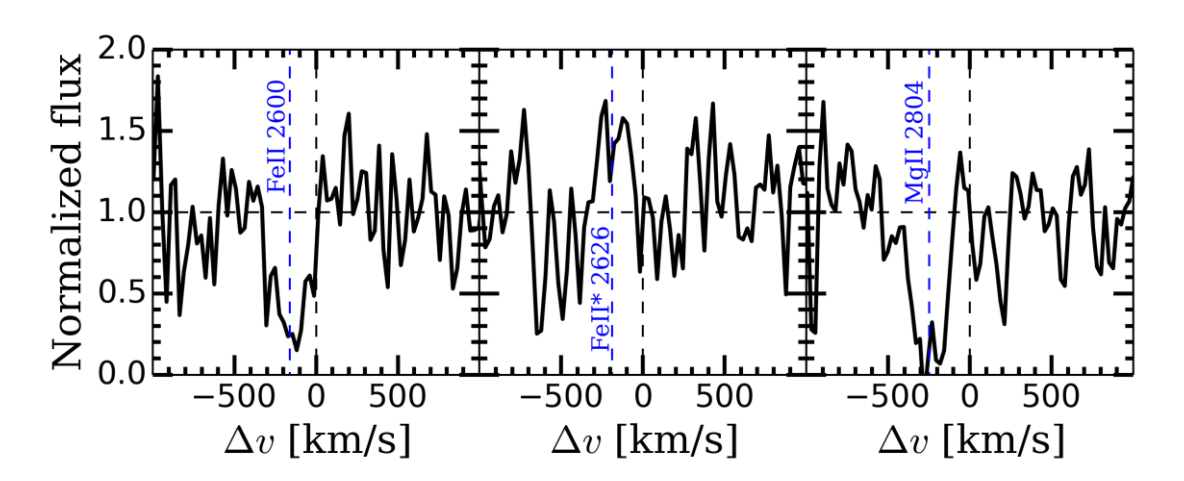


Figure **4**: The blueshifted FeIIλ2600 absorption (left), FeII\*λ2626 fine-structure emission (middle), and MgIIλ2804 absorption lines (right) of OIIIB-1. The blue vertical dashed lines indicate the centroids of velocity offsets of each line. Yuma et al. (2019)

## e. Discovery of a giant Green Pea (GP) at z=0.838

Among for [OIII] blobs at z~0.7, we discover a giant GP, OIIIB-4, which has spatially extended [OIII] emission and line ratios consistent with those of the green peas found at z=0.1—0.4 by Cardamone et al. (2009). The green pea is a name for a special type of compact galaxies with extremely strong [OIII] emission line with the rest-frame [Oiii] equivalent width up to 1000 Å. Figure 5 shows the close-up RGB image of OIIIB-4. The extended green color in the order of 10—20 kpc around the center of OIIIB-4 clearly indicates the large-scale extension of the [OIII] emission line.

The giant GP discovered in this TRF project is a crucial evidence that challenges the conventional picture that star-forming galaxies with extreme emission lines are typical compact. The spectroscopic results of [OIII] blobs at z~0.7 including the discovery of the giant GP are summarized and published in The Astrophysical Journal (Yuma et al. 2019, ApJ, 882, 17, 1-16).

### f. Proposals to request observing time at world-class telescopes

In addition to one paper in Q1, I am submitting three research proposals in three different topics using the results this TRF project to three astronomical observatories around the world. As a result of this TRF project, I have new collaboration at University of Melbourne to propose the astronomical observation to the Anglo-Australian Telescope in Australia. In addition, with collaboration with The University of Tokyo and UC Santa Barbara, I submitted the proposals to Subaru telescope and Keck telescope in Hawaii, USA. If the proposals are approved, we will be able to study the physical properties of these unique objects in details.

### Conclusion

Galaxies in the universe can be largely divided into two populations: young, star-forming spiral galaxy, and old, passively evolving elliptical galaxy. It has been long known that a spiral galaxy stops forming new stars and eventually turns into the elliptical one at some point in the universe. However, the physical mechanism responsible for quenching the star formation process is still unclear. Gas outflow at large scale is considered one of the plausible scenarios. This project aims to study the evolution of the large-scale outflow at each epoch of the universe and ultimately to understand the quenching process that turns star-forming galaxies into the elliptical ones. To do so, I conduct the systematic survey of galaxies exhibiting large-scale outflow at redshifts of z=0.1-1.5 covering the past 9 billion years of the universe.

I started with creating the photometric catalogs of both stars and galaxies in the Subaru XMM Deep Survey (SXDS) and COSMOS fields. According to the expansion of the universe, light from distant galaxies is shifted redward, which is so called "redshift." The galaxies with strong [OII]3727, [OIII]5007, or Ha6563 emission lines at different redshifts are then identified with the narrowband technique that uses the filter with a narrow wavelength width of about 100 Å to detect the emission lines. I select 430 galaxies in total at z=0.4-1.5 with spatially extended [OII], [OIII], or Ha emission lines, which I call [OII], [OIII], or Ha blobs, respectively. The number of blobs candidates significantly increases from the previous survey conducted in 2017 (Yuma et al. 2017). I develop a new selection method that is able to securely select galaxies with genuine extension of gas emission. The extended emission beyond the stellar component of the galaxy is thought to be hot metal-rich gas flowing out of the galaxy rather than pristine gas inflowing from the metal-poor intergalactic medium. The galactic-scale outflow is thought to be fueled by either stellar feedback from supernova or feedback from active galactic nuclei (AGN). The physical properties of 4 [OIII] blobs at z=0.83 are studied in details with the spectroscopic observations with Subaru/FOCAS. One of them, named a giant green pea, shows remarkably high [OIII]/[OII] ratio in the range of 5-10 over 14 kpc. It is indicated that this giant green pea has a high ionization parameter. It is possible that the

spatially extended [OIII] emission of the giant green pea is originated from outflowing gas produced by the intense star forming activity in a density-bounded ionization state of the galaxy. This result just confirms that the selection method I have introduced is efficient in isolating the galaxy with large-scale outflowing gas. Further spectroscopic observations will be carried out after this project to investigate the physical conditions of outflowing gas expelled out the galaxy. The study will eventually lead to the understanding of galaxy formation and evolution as a function of time since the beginning of the universe.

# ข้อเสนอแนะสำหรับงานวิจัยในอนาคต

ในงานวิจัยนี้ ถึงแม้เราสามารถหาได้ว่าที่แต่ละช่วงอายุของจักรวาลนั้น มีกาแล็กซี่ที่ ปลดปล่อยก๊าซออกเป็นบริเวณกว้างเท่าไร แล้วกาแล็กซี่เหล่านี้กำลังเปลี่ยนเป็นกาแล็กซี่ที่ไม่ สร้างดาวอีกแล้วหรือไม่ แต่เรายังไม่สามารถเปรียบเทียบหาวิวัฒนาการของกาแล็กซี่เหล่านี้ เทียบกันหลายๆ ช่วงอายุของจักรวาลได้ เนื่องจากการสำรวจของเรายังมีขนาดเล็กเกินไป หนทางในการทำวิจัยในอนาคต คือ การขยายการสำรวจออกไปให้ครอบคลุมพื้นที่มากขึ้น โดย ตัวผู้ทำวิจัยนี้ ได้ขอทุนพัฒนาศักยภาพอาจารย์รุ่นใหม่ของสกว.อีกรอบ เพื่อสานต่องานวิจัยนี้ให้ สมบูรณ์แบบมากขึ้น

# Output จากโครงการวิจัยที่ได้รับทุนจาก สกว.

- 1. ผลงานตีพิมพ์ในวารสารวิชาการนานาชาติ (ระบุชื่อผู้แต่ง ชื่อเรื่อง ชื่อวารสาร ปี เล่มที่ เลขที่ และหน้า) หรือผลงานตามที่คาดไว้ในสัญญาโครงการ
  - 1.1 S. Yuma, M. Ouchi, S. Fujimoto, T. Kojima, Y. Sugahara, "A Giant Green Pea Identified in the Spectroscopy of Spatially Extended [OIII] Sources," The Astrophysical Journal, 882, 17, 1-16, 2019 (Q1; Impact Factor: 5.580)

# 2. การนำผลงานวิจัยไปใช้ประโยชน์

- 2.1 เชิงวิชาการ (มีการพัฒนาการเรียนการสอน/สร้างนักวิจัยใหม่)
  - 2.1.1 กาแล็กซี่ที่ค้นพบในงานวิจัยครั้งนี้ สามารถใช้เป็นตัวอย่างเพื่อศึกษา ต่อยอดลงไปในรายละเอียดของตัวกาแล็กซี่แต่ละกาแล็กซี่ได้ ซึ่งทำให้ เรามีความเข้าใจในกระบวนการเกิดการปลดปล่อยก๊าซของกาแล็กซี่ได้ มากขึ้น
  - 2.1.2 มีนักศึกษาระดับปริญญาโทเอกของมหาวิทยาลัยมหิดล จำนวน 3 คน และระดับปริญญาตรีของมหาวิทยาลัยเทคโนโลยีสุรนารี จำนวน 1 คน ได้เข้ามาร่วมทำวิจัยในหัวข้อนี้ ตรงนี้นับเป็นการเพิ่มประสบการณ์ใน

# การทำวิจัยและเตรียมความพร้อมให้กับนักศึกษาเพื่อจะนำไปใช้ใน การศึกษาต่อขั้นสูงต่อไป

3. อื่นๆ (เช่น ผลงานตีพิมพ์ในวารสารวิชาการในประเทศ การเสนอผลงานในที่ประชุมวิชาการ หนังสือ การจดสิทธิบัตร)

ระงับไป

3.1 วิทยากรพิเศษบรรยายในหัวข้อ "Systematic Survey for Star-forming Galaxies with Spatially Extended Emission Lines" ณ วิทยาลัยเพื่อการ คันคว้าระดับรากฐาน มหาวิทยาลัยนเรศวร วันที่ 11 ก.ค. 2562
3.2 เนื่องด้วยสถานการณ์ Covid-19 ในขณะนี้ (เมษายน 2563) ทำให้แผนการ ไปเสนอผลงานชิ้นนี้ในงานประชุมทางวิชาการและมหาวิทยาลัยต่างๆ ต้อง



# A Giant Green Pea Identified in the Spectroscopy of Spatially Extended [O III] Sources

Suraphong Yuma <sup>1</sup> <sup>1</sup> <sup>1</sup> <sup>1</sup> <sup>1</sup> Masami Ouchi <sup>2</sup> <sup>1</sup> <sup>1</sup> <sup>1</sup> <sup>1</sup> <sup>1</sup> Department of Physics, Faculty of Science, Mahidol University, Bangkok 10400, Thailand; suraphong.yum@mahidol.ac.th <sup>2</sup> Institute for Cosmic Ray Research, The University of Tokyo, Kashiwa-no-ha, Kashiwa 277-8582, Japan <sup>3</sup> Department of Astronomy, University of Tokyo, Hongo, Bunkyo-ku, Tokyo 113-0033, Japan <sup>4</sup> Department of Physics, University of Tokyo, Hongo, Bunkyo-ku, Tokyo 113-0033, Japan Received 2019 April 25; revised 2019 June 13; accepted 2019 July 2; published 2019 August 27

### **Abstract**

We present the results of the deep Subaru/FOCAS and Keck/MOSFIRE spectroscopy for four spatially extended  $[O III] \lambda\lambda 4959$ , 5007 sources, dubbed [O III] blobs, at z = 0.6–0.8 that are originally pinpointed by large-area Subaru imaging surveys. The line diagnostics of the rest-frame optical lines suggests that only one [O III] blob, OIIIB-3, presents an active galactic nucleus (AGN) signature, indicating that hot gas of the rest of the [O III] blobs is heated by star formation. One of such star-forming [O III] blobs, OIIIB-4, at z = 0.838 has an [O III] equivalent width of 845  $\pm$  27 Å and an [O III]-to-[O II]  $\lambda\lambda$ 3726, 3729 ratio of [O III]/[O II] = 6.5  $\pm$  2.7, which are as high as those of typical Green Peas. The spatially resolved spectrum of OIIIB-4 shows [O III]/[O II] = 5-10 over 14 kpc in the entire large [O III] extended regions of OIIIB-4, unlike the known Green Peas, whose strong [O III] emission region is compact. Moreover, OIIIB-4 presents no high-ionization emission lines, unlike Green Beans, which have extended [O III] emission with a type 2 AGN. OIIIB-4 is thus a giant Green Pea, which is a low stellar mass  $(7 \times 10^7 M_{\odot})$  galaxy with a very high specific star formation rate (sSFR =  $2 \times 10^2$  Gyr<sup>-1</sup>), a high-ionization parameter  $(q_{\rm ion} \sim 3 \times 10^8 \, {\rm cm \, s}^{-1})$ , and a low metallicity similar to those of Green Peas. Neither an AGN light echo nor a fast radiative shock likely takes place owing to the line diagnostics for spatially resolved components of OIIIB-4 and no detections of He II  $\lambda$ 4686 or [Ne V]  $\lambda\lambda$ 3346, 3426 lines that are fast radiative shock signatures. There is a possibility that the spatially extended [O III] emission of OIIIB-4 is originated from outflowing gas produced by the intense star formation in a density-bounded ionization state.

Key words: galaxies: evolution - galaxies: formation - galaxies: high-redshift - galaxies: ISM - ISM: jets and outflows

### 1. Introduction

A galaxy is not a closed box that can evolve itself without exchanging materials with the environment. The accretion of cooled gas onto the galaxy is important for the galaxy to form new stars in the  $\Lambda$  cold dark matter ( $\Lambda$ CDM) model. However, the inflow alone would cause an overestimation of star formation at both low-mass and high-mass ends (e.g., Bell et al. 2003; Mutch et al. 2013). The feedback mechanism involving gas outflows becomes a default tool to resolve the discrepancy in hydrodynamic simulations (e.g., Benson et al. 2003; Somerville et al. 2008; Oppenheimer et al. 2010; van de Voort et al. 2011). The evolutional state of a galaxy is thus thought to depend on the balance of the gas flows in and out of the galaxy (e.g., Lilly et al. 2013). In addition, the galacticscale outflow is considered a solution for various observational phenomena, including regulating the main sequence of galaxies on the mass-SFR (star formation rate) diagram (e.g., Noeske et al. 2007) and the mass-metallicity relation (e.g., Tremonti et al. 2004) and enriching the chemical abundance of interstellar medium (ISM) and intergalactic medium (IGM; e.g., Martin 2005; Rupke et al. 2005a, 2005b; Weiner et al. 2009; Coil et al. 2011).

Outflows have been massively studied in several types of galaxies ranging from normal star-forming galaxies (e.g., Weiner et al. 2009; Steidel et al. 2010; Erb et al. 2012; Martin et al. 2012; Bradshaw et al. 2013; Rubin et al. 2014) and submillimeter galaxies (e.g., Alexander et al. 2010) to more extreme systems like radio galaxies (e.g., Nesvadba et al. 2008; Liu et al. 2013), ultraluminous infrared galaxies (e.g., Heckman et al. 1990; Martin 2005; Rupke et al. 2005a, 2005b; Soto et al.

2012), and active galactic nuclei (AGNs; e.g., Cicone et al. 2014; Cheung et al. 2016; Rupke et al. 2017). Outflows are found to be ubiquitous in galaxies with an SFR surface density larger than  $\sim 0.1\,M_\odot\,{\rm yr}^{-1}\,{\rm kpc}^{-2}$  and become stronger in more massive star-forming galaxies with higher SFRs (Heckman et al. 2000; Martin 2005; Weiner et al. 2009; Kornei et al. 2012; Martin et al. 2012). In the case of AGNs, the outflows strongly correlate with the black hole mass ( $M_{\rm BH}$ ) in that the mass outflow rate increases with increasing  $M_{\rm BH}$  (Rupke et al. 2017). An active supermassive black hole alone could fuel the large-scale outflow even in a low-luminosity AGN (Cheung et al. 2016).

Most of these studies are based mainly on the optical/nearinfrared (NIR) spectroscopic observations of blueshifted interstellar absorption lines such as Na I  $\lambda\lambda$ 5890, 5896, Mg II  $\lambda\lambda$ 2796, 2803, Fe II  $\lambda$ 2374, and Fe II  $\lambda$ 2383 to indicate the outflow signature. No systematic search had been done by using only the imaging data until Yuma et al. (2013) proposed to use the narrowband technique to systematically identify the gas outflowing galaxies by selecting star-forming galaxies with the strong [O II]  $\lambda\lambda$ 3726, 3729 emission line spatially extended over 30 kpc beyond the stellar components. They called this [O II] extended object an "[O II] blob," or in short "O IIB." The spatial extension of a metal line like the [O II] emission line that is redshifted and falls into the narrowband image might indicate a large-scale outflow beyond the galaxy rather than evidence of a gas inflow from the metal-poor IGM (e.g., Aguirre et al. 2008; Fumagalli et al. 2011). Yuma et al. (2013) successfully identified 12 O IIBs at  $z \sim 1.2$ , one of which is classified as an obscured AGN. The others are potentially normal star-forming

galaxies, as they are not detected in X-ray or radio 1.4 GHz wavelengths. The hypothesis that the extended [O II] emission line may represent the outflow from the [OII] blobs is spectroscopically confirmed by the traditional method of detecting blueshifted interstellar absorption lines (Yuma et al. 2013; Harikane et al. 2014). The systematic search was then expanded toward lower and higher redshifts, i.e., z = 0.1-1.5(Yuma et al. 2017). In Yuma et al. (2017), the spatially extended emission lines include [O II]  $\lambda\lambda 3726$ , 3729, [O III]  $\lambda$ 5007, and H $\alpha$   $\lambda$ 6563. The resulting sample is named accordingly as an [O II] blob (O IIB), an [O III] blob (O IIIB), and an H $\alpha$  blob (HAB). They found 77 blobs at z=0.4-1.5 in total, eight of which are likely to be powered by AGNs. It is suggested that the blobs are mostly normal star-forming galaxies. It is of interest to investigate an energy source for the extended emission lines of the blobs that are identified as normal star-forming galaxies.

Galaxies with large extensions of emission lines have recently been discovered by many studies. Lin et al. (2017) discovered a giant  $H\alpha$  blob with an  $H\alpha$  extent of 3–4 kpc in radius. The spatial extension of the [O III] emission line is also found (Brammer et al. 2013; Sun et al. 2017). An AGN is thought to be a primary source of energy to produce the large-scale outflow in both the  $H\alpha$  blob discovered by Lin et al. (2017) and the [O III] blobs studied by Sun et al. (2017). The latter work suggested that the size of the [O III] extension strongly correlates with the AGN luminosity. Sun et al. (2017) also argued that there is no AGN luminosity threshold for launching the outflow, which is consistent with Cheung et al. (2016). This means that it is common to see the extended emission line in all AGNs regardless of their luminosities.

Although there are certain detailed studies about the extended emission lines in the normal star-forming galaxies (e.g., Genzel et al. 2011; Newman et al. 2012a, 2012b), the physical mechanism responsible for the spatially extended emission lines beyond the stellar component of the galaxies is still not well understood. To date, many studies about the ISM of galaxies are conducted with the integral field unit (IFU) observations (e.g., Förster Schreiber et al. 2009, 2014; Lin et al. 2017; Sun et al. 2017). This 3D imaging spectrograph enables researchers to investigate the spectra of the entire galaxies simultaneously with 2D imaging. In this paper, instead of using the IFU, we take a simple step by observing the [O III] blobs at z = 0.63 and z = 0.83 that show no AGN signature in X-ray and radio wavelengths originally selected by Yuma et al. (2017) with a spectrograph in the multiobject spectroscopy mode. By designing the slit direction to cover the longest extension of the emission lines of the blobs, we are able to determine the emission-line ratios and examine the physical properties of the extended component of the emission lines along the slit direction.

In Section 2, we discuss the [O III]-blob targets for the spectroscopic observations. Section 3 describes details of both optical and NIR observations and data reduction processes. We then report the results of systematic redshifts, outflow signature, AGN contribution, and properties of the ISM, including the radial profile of the [O III] blobs, in Section 4. We also report the discovery of a giant Green Pea in this section. In Section 5, we discuss the plausible scenarios that could be responsible for the spatial extension of the emission lines seen in the [O III] blobs. The last section, Section 6, is the summary of all our findings. Throughout this paper, we adopt the

standard  $\Lambda$ CDM cosmology with  $H_0 = 70 \,\mathrm{km \, s^{-1} \, Mpc^{-1}}$ ,  $\Omega_m = 0.3$ , and  $\Omega_{\lambda} = 0.7$ . All magnitudes are given in the AB system (Oke & Gunn 1983).

### 2. Targets for Spectroscopy

We conduct the spectroscopic observations of four [O III] blobs at  $z \sim 0.63$  and  $z \sim 0.83$ . Our spectroscopic sample is originally identified as an [O III] blob by Yuma et al. (2017). They conducted the systematic survey of [O II], [O III], and  $H\alpha$ blobs at z = 0.1-1.5, i.e., star-forming galaxies with strong [O II], [O III], and H $\alpha$  emission lines, respectively, spatially extended over 30 kpc. The emission-line extension is measured z = 0.1-1.5 found by Yuma et al. (2017), there are 4 and 13 [O III] blobs at z = 0.63 and z = 0.83, respectively. All blobs are cross-matched with the X-ray and radio catalogs to primarily check for the AGN existence. The X-ray source catalog is obtained from Ueda et al. (2008). It is observed with the European Photon Imaging Camera (Strüder et al. 2001; Turner et al. 2001) on the XMM-Newton telescope (Jansen et al. 2001). The flux limits of the catalog are  $6 \times 10^{-16}$ ,  $8 \times 10^{-16}$ ,  $3 \times 10^{-15}$ , and  $5 \times 10^{-15}$  erg s<sup>-1</sup> cm<sup>-2</sup> in the 0.5-2 keV, 0.5-4.5 keV, 2-10 keV, and 4.5-10 keV bands, respectively. These flux limits approximately correspond to the X-ray luminosities of  $10^{42} \, {\rm erg \, s^{-1}}$  at  $z \sim 0.7$ . The radio catalog is from Simpson et al. (2006). The radio data are observed with the Very Large Array in 1.4 GHz down to the limit of 100  $\mu$ Jy. All of the [O III] blobs are not detected in X-ray and radio wavelengths.

The criteria of the spectroscopic targets are that (1) they are among the [O III] blobs with the largest extension of the [O III] emission line and/or (2) they are located close to each other so that we can maximize the number of the [O III] blobs observed within one mask. As a result, we select four [O III] blobs as the spectroscopic targets and observe them with two masks. The targets are OIIIB063s-1, OIIIB063s-2, OIIIB083m-2, and OIIIIB083m-12. The IDs are from the original catalog by Yuma et al. (2017). O IIIB indicates that it is an [O III] blob, a galaxy with the extended [O III] emission line. Three numbers after O IIIB represent the redshifts; for example, 063 means that the blob is at z = 0.63. The letter "s" or "m" stands for single or multiple, respectively, indicating the number of stellar components in one blob. The last numbers show the order of blobs, starting from "1" for the blob with the largest extension of the emission line. To avoid any confusion, we hereafter refer to OIIIB063s-1, OIIIB063s-2, OIIIB083m-2, and OIIIIB083m-12 as O IIIB-1, O IIIB-2, O IIIB-3, and O IIIB-4, respectively. Figure 1 shows the 2D images of the [O III] emission line, the stellar continuum, and the equivalent width (EW) map of our four targets. The emission-line images (NB - BB) correspond to the NB816-Rz and NB921-z' images for the [O III] blobs at z = 0.63 and z = 0.83, respectively, where Rz is defined as Rz  $\equiv (R+2 z')/3$ . The contour of the [O III] extension is also displayed in the figure. The slit direction with the exact width and length is shown in the right panel of Figure 1. Coordinates and photometric properties of these four [O III] blobs derived by Yuma et al. (2017) are listed in Table 1.

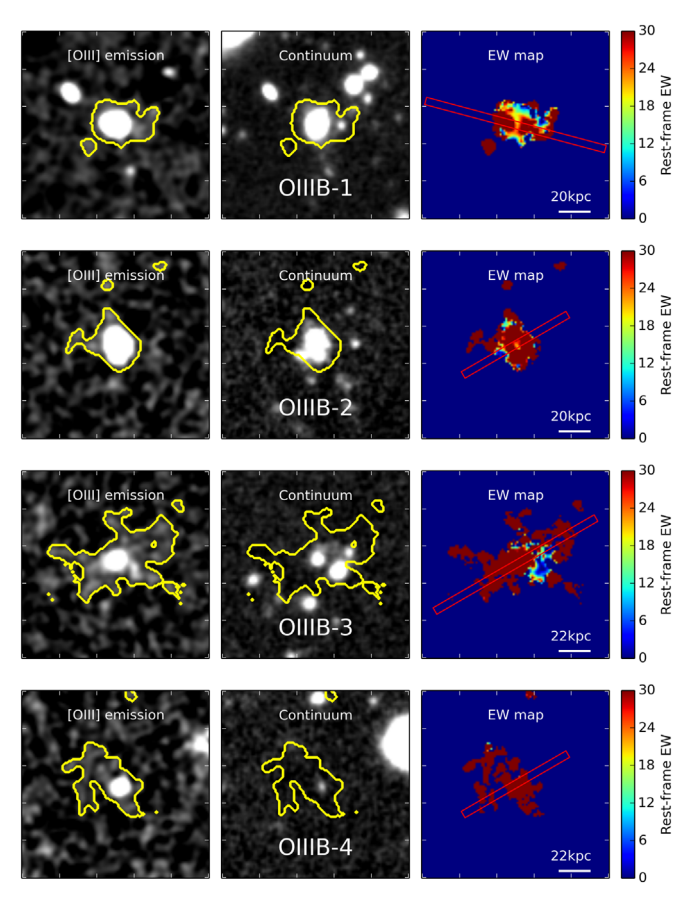


**Figure 1.** From left to right: emission-line (NB - BB), stellar continuum, and EW maps of four [O III] blobs at z = 0.63 and z = 0.83, respectively. The emission-line images are NB816-Rz and NB921-z' for the blobs at z = 0.63 and z = 0.83, respectively. Rz is defined as  $Rz \equiv (R+2z')/3$ . IDs are indicated in the middle panel. North is up and east is to the left. Yellow contours in the left and middle panels indicate the isophotal area of the emission-line flux measured down to  $1.2 \times 10^{-18} \, {\rm erg \, s^{-1} \, cm^{-2} \, arcsec^{-2}}$ . The color bar in the right panel corresponds to the rest-frame EW per pixel. The magenta rectangle shows the slit direction that we used to observe the spectrum of the [O III] blobs with Subaru/FOCAS.

### 3. Observation and Data Reduction

### 3.1. Subaru/Faint Object Camera and Spectrograph (FOCAS)

We conducted the optical spectroscopic follow-up observations with Subaru/FOCAS (Kashikawa et al. 2002) on 2014 October 21-22 and 2015 December 2-4 (S14B-130 and S15B-059; PI: S. Yuma). Details about the Subaru/FOCAS spectroscopic observations are described in Yuma et al. (2017). Briefly speaking, we performed the observations in the multiobject spectroscopy (MOS) mode with the VPH450 grating and the VPH850 grating with the SO58 order-cut filter. The gratings cover 3800-5250 Å with a dispersion of 0.37 Å pixel<sup>-1</sup> and 5800–10500 Å with 1.17 Å pixel<sup>-1</sup>, respectively. We adopted the slit width of 0."8, providing the spectral resolutions of 1700 and 750 for VPH450 and VPH850+SO58, respectively. We used two MOS masks to observed four [O III] blobs. Mask1 contains only O IIIB-1, which is the largest [O III] blob at z = 0.63, while the other three blobs (O IIIB-2, O IIIB-3, and O IIIB-4) are so close to each other that we can place them all in Mask2. The on-source exposure times for Mask1 are 180 and 120 minutes in VPH450 and VPH850+SO58, respectively. For Mask2, the exposure times are 260 and 100 minutes. The sky when we observed the target in Mask1 was quite clear in that we obtain the seeing size of  $\sim 0.0^{\circ}6-0.0^{\circ}7$ . Unfortunately, the weather was getting worse when we observed Mask2. The seeing size is roughly  $\sim 0.0^{\circ}9$ . We carefully designed the slit direction to cover the longest extent of the [O III] emission line as shown with the magenta color in Figure 1. Note that, in Mask2, we intended to do so with O IIIB-3, which is the second-largest [O III] blob at z=0.83. Because all slits in one mask are required to arrange in the identical direction, the slit directions for O IIIB-2 and O IIIB-4 are consequently not oriented to the longest extension of their [O III] emission lines.

Data reduction has been carried out with the FOCASRED package, which is the specific pipeline on the Imaging Reduction and Analysis Facility for Subaru/FOCAS data reduction. We started with bias subtraction, flat-fielding, and distortion correction. Wavelength calibration is then performed by using the ThAr lamp and OH airglow emission lines for VPH450 and VPH850+SO58 spectra, respectively. After we subtracted the sky background, we stacked the spectra and extracted them along the spatial direction to create 1D spectra. The extracting width is designed to cover the entire spatial extension of the emission line. Flux calibration is carried out by using the standard star G191-B2B observed with the same slit width. It is extracted to the 1D spectrum with the same extraction width as the target. The slit loss is automatically corrected during the flux calibration process. The  $3\sigma$  flux limits are summarized in Table 2.

### 3.2. Keck/MOSFIRE

NIR observation was conducted only for O IIIB-1 with MOS For Infrared Exploration (MOSFIRE; McLean et al. 2012) attached on the Keck I telescope. O IIIB-1 was observed as a filler target with the *Y*-band filter on 2014 January 3–4 (S15B-075; PI: M. Ouchi). The main objective of the MOSFIRE proposal is to confirm the Ly $\alpha$  emitters at  $z \sim 5.7$ . The spectral resolution is 3388 with the standard 0."7 slit width. The total exposure time is 4.45 hr with a seeing size of  $\sim$ 0."7. Data reduction is performed with the MOSFIRE data reduction pipeline<sup>5</sup> following the standard processes for reducing the spectra and flux calibration with the standard stars taken during the observations. The exposure time and the limiting flux are also listed in Table 2.

### 4. Results

### 4.1. Systemic Redshifts

Before we investigate the spectra in detail, we first check whether our [O III] blob sample is at the targeted redshifts. We examine the emission lines detected in the VPH850+SO58 spectra. The [O III] blobs at  $z\sim0.63$  and  $z\sim0.83$  are originally identified by the narrowband technique using the NB816 and NB921 images, respectively. Thus, we expect the [O III] emission line to be around 8090–8210 Å for O IIIB-1 and O IIIB-2 and 9130–9262 Å for O IIIB-3 and O IIIB-4. In fact, Yuma et al. (2017) already confirmed that the emission line detected in the wavelength ranges mentioned above is [O III]  $\lambda$ 5007 based on the spectroscopic confirmation of [O II]  $\lambda$ 3727, H $\beta$   $\lambda$ 4861, and [O III]  $\lambda$ 4959 emission lines at the corresponding wavelengths. They confirmed that O IIIB-1 and O IIIB-2 are at z=0.621 and z=0.641, respectively, whereas O IIIB-3 and O IIIB-4 are both at z=0.838. We fit the

https://keck-datareductionpipelines.github.io/MosfireDRP/

Table 1
Photometric Properties of [O III] Blobs at z = 0.63 and z = 0.83 for Spectroscopic Follow-up

Object Name	α (J2000)	δ (J2000)	NB - BB (mag)	$L([O III])^a$ $(10^{41} \text{ erg s}^{-1})$	Isophotal Area (kpc²)
		[O III] Blobs at z	= 0.63		
O IIIB-1 (OIIIB063s-1) O IIIB-2 (OIIIB063s-2)	02 17 50.244 02 19 05.902	-05 00 04.159 -05 13 48.599	$\begin{array}{c} 22.04 \pm 0.14 \\ 22.27 \pm 0.15 \end{array}$	$\begin{array}{c} 4.99\pm0.7 \\ 4.04\pm0.7 \end{array}$	1121.2 1121.2
		[O III] Blobs at z	= 0.83		
O IIIB-3 (OIIIB083m-2) O IIIB-4 (OIIIB083m-12)	02 19 03.734 02 18 58.701	-05 11 53.243 -05 12 58.126	$22.77 \pm 0.13 \\ 23.32 \pm 0.23$	$4.40 \pm 0.6 \\ 2.64 \pm 0.6$	1675.0 981.9

#### Note.

Table 2 Details of Optical and Near-infrared Spectroscopic Observations for Four [O III] Blobs at z=0.63 and z=0.83

Ins./Grating+Filter	Exposure Time (minutes)	$3\sigma$ Flux Limit (erg s <sup>-1</sup> cm <sup>-2</sup> )
Mask1: O IIIB-1		
FOCAS/VPH450	180	$\simeq 3.8 \times 10^{-17}$
FOCAS/VPH850+SO58	120	$\simeq 1.1 \times 10^{-18}$
MOSFIRE/Y	285	$\simeq 3.1 \times 10^{-18}$
Mask2: O IIIB-2, O IIIB-3, and	О ШВ-4	
VPH450	260	$\simeq 1.1 \times 10^{-17}$
VPH850+SO58 <sup>a</sup>	100	$\simeq 1.0 \times 10^{-18}$

#### Note.

[O II], H $\beta$ , and [O III] emission lines with a single Gaussian profile and adopt the center of the Gaussian profile that is best fitted to the [O III]  $\lambda$ 5007 emission line as the spectroscopic redshift for each [O III] blob (Table 3). Our resulting spectroscopic redshifts are consistent with those derived by Yuma et al. (2017).

## 4.2. Spectroscopic Properties of Emission Lines

The Subaru/FOCAS spectra of four [O III] blobs at  $z \sim 0.63-0.83$  are illustrated in Figure 2 at the observed wavelengths of the [O II]  $\lambda$ 3727,  $H\beta \lambda 4861$ , [O III]  $\lambda\lambda4959$ , 5007 emission lines. In each plot, we show the 2D spectral image in the top panel and the 1D spectrum in the bottom one. All the lines for a given blob are plotted with the same flux scale to provide the idea of the strength of the emission lines as compared to one another. The top row of Figure 2 shows that the stellar continuum is significantly detected in O IIIB-1. The excessive extension of the emission lines beyond the stellar components is clearly seen in the 2D spectral image.

Although we marginally detect the stellar continuum of O IIIB-2, the emission lines of O IIIB-2 seem to be extended over the stellar continuum in the spatial direction. Likewise, we are able to see the spatial extension of the [O III]  $\lambda 5007$  emission line of O IIIB-3. O IIIB-3 shows the significantly larger spectral line width of the [O III]  $\lambda 5007$  emission as

Table 3 Spectroscopic Redshifts and Dust-corrected Fluxes of [O II], H $\beta$ , and [O III] Emission Lines for Four [O III] Blobs at z=0.63–0.83

Target	Zspec	Observed Flux (×10 <sup>-16</sup> erg s <sup>-1</sup> cm <sup>-2</sup> )		
	[O II]	$_{\mathrm{H}\beta}$	[O III]	
O IIIB-1	0.6210	$16.67 \pm 0.29$	$5.02 \pm 0.27$	$12.16 \pm 0.25$
O IIIB-2	0.6413	$7.33 \pm 0.60$	$1.53 \pm 0.31$	$3.58\pm0.65$
O IIIB-3	0.8365	$6.12 \pm 0.51$	$0.71\pm0.35$	$5.48\pm0.68$
O IIIB-4	0.8379	$0.31 \pm 0.11$	$0.30\pm0.12$	$2.02\pm0.12$

compared with O IIIB-1 and O IIIB-2. The FWHM of the [O III]  $\lambda$ 5007 line of O IIIB-3 is 419.5  $\pm$  76.8 km s<sup>-1</sup> after correcting for the instrument, while it is on the order of  $150-200 \,\mathrm{km \, s^{-1}}$  for O IIIB-1 and O IIIB-2. For O IIIB-4, the stellar continuum is unfortunately not detected, but we can detect the [O III] emission line with the high signal-to-noise ratio (S/N). However, the [O II] and H $\beta$  emission lines are marginally detected with an S/N of  $2\sigma$ – $3\sigma$ . The observed flux of each emission line is derived by fitting the 1D spectrum with a single Gaussian profile and corrected for the dust attenuation, which is explained in the Appendix. In short, we derive the dust attenuation of OIIIB-1 and OIIIB-2 from the Balmer decrement using the  $H\gamma/H\beta$  line ratios. We find that the color excesses (E(B-V)) estimated from the Balmer decrement are in agreement with those derived by fitting the observed spectral energy distribution of the blob with the stellar population synthesis models (SED fitting method; Appendix). Therefore, for O IIIB-3 and O IIIB-4, whose H $\gamma$  emission lines are not detected, we adopt the color excesses derived by the SED fitting method. The nebular color excesses of O IIIB-3 and O IIIB-4 are then calculated by using the relation between the nebula and the stellar dust extinctions in Calzetti et al. (2000). More details on the SED fitting procedures of the [O III] blobs are explained in Section 4.7 and Yuma et al. (2017). We summarize the dust-corrected fluxes of the  $[O II] \lambda 3727$ ,  $H\beta \lambda 4861$ , and [O III]  $\lambda 5007$  emission lines with corresponding  $1\sigma$  uncertainties in Table 3. The extended features seen in O IIIB-1, O IIIB-2, and O IIIB-3 confirm that the blob selection method by Yuma et al. (2017) is efficient in selecting galaxies with the spatially extended emission line.

### 4.3. Outflow Signature

The galaxies with spatially extended emission lines like [O III] blobs are thought to be in an ongoing process of the large-scale outflow. The gas outflow is already confirmed in

<sup>&</sup>lt;sup>a</sup> The luminosity of the [O III] emission lines is derived from the magnitude in NB - BB and is not corrected for internal dust attenuation.

<sup>&</sup>lt;sup>a</sup> For O IIIB-2, we discard two observed frames to avoid the cosmic ray at the wavelength of the H $\beta$   $\lambda$ 4861 emission line. Therefore, the  $3\sigma$  flux limit of O IIIB-2 is  $\simeq 3.7 \times 10^{-18}$  erg s<sup>-1</sup> cm<sup>-2</sup>.

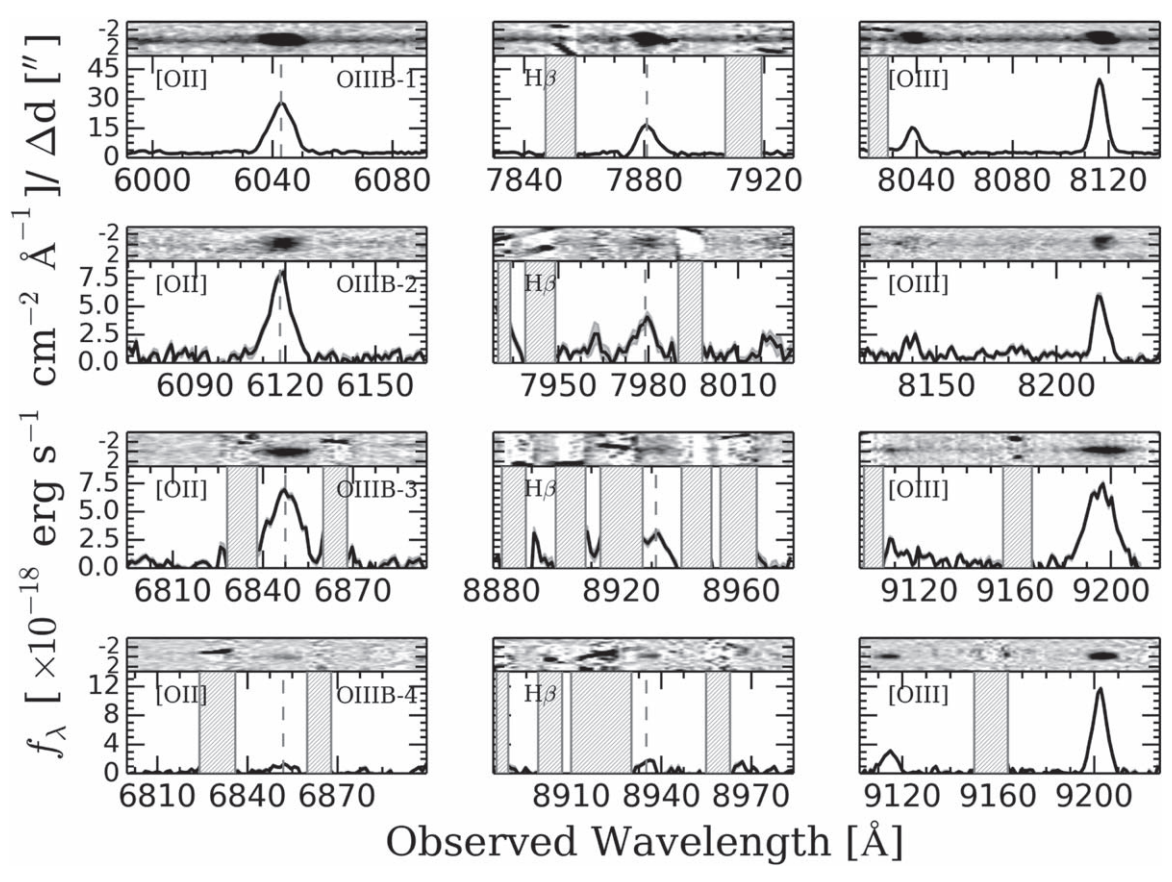


Figure 2. Subaru/FOCAS spectra of O IIIB-1, O IIIB-2, O IIIB-3, and O IIIB-4 from top to bottom, respectively. The left, middle, and right columns show the [O II],  $H\beta$ , and [O III] emission lines of each object, respectively. In each plot, we illustrate the 2D spectrum in the top panel, centering at the center of the stellar component of the blob, while the bottom panel shows the 1D spectrum at the corresponding observed wavelengths. The centers of [O II] and  $H\beta$  lines are indicated with the dashed gray lines. The shaded regions in some figures indicate the area with poor S/N in the spectrum.

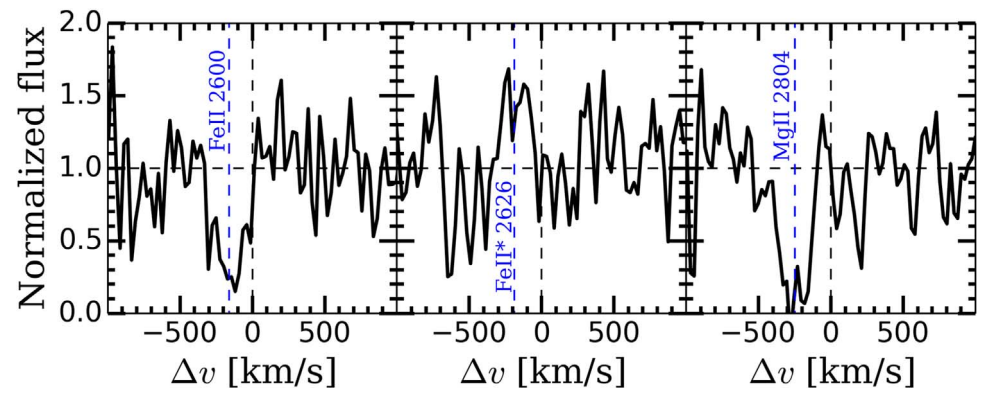


Figure 3. Blueshifted Fe II  $\lambda$ 2600 absorption (left), Fe II\*  $\lambda$ 2626 fine-structure emission (middle), and Mg II  $\lambda$ 2804 absorption lines (right) of O IIIB-1. The observed flux is normalized to the continuum spectrum. The blue vertical dashed lines indicate the centroids of velocity offsets of each line.

[O II] blobs at  $z\sim1.2$  with Subaru/FOCAS, VLT/VIMOS, and Magellan/LDSS spectra of the [O II] blobs at  $z\sim1.2$  (Yuma et al. 2013; Harikane et al. 2014); however, this is the first time to confirm whether the [O III] blobs are in the middle of the outflow process. The blueshifted interstellar absorption lines are one of the most common methods that are used to study the outflow process of the galaxies. Unfortunately, the spectra of three out of four blobs in the VPH450 grating, in which we expect to detect the absorption lines, have too low S/N. We only detect the absorption lines in the O IIIB-1 spectrum. Figure 3 shows the blueshifted Fe II  $\lambda$ 2600 absorption, Fe II\*  $\lambda$ 2626 fine-structure emission, and Mg II  $\lambda$ 2804 absorption lines.

They are all blueshifted from the systemic redshift, indicating the gas outflow from the galaxy. We fit the blueshifted absorption and emission lines with a single Gaussian profile. The velocity offsets of the Fe II, Fe II\*, and Mg II lines are -160, -200, and -270 km s $^{-1}$ , respectively. It is important to note that the Mg II absorption line is possibly affected by strong resonant emission at the systemic velocity. This infilling emission can shift the centroid of the Mg II velocity offset on the order of tens of kilometers per second (e.g., Prochaska et al. 2011). Erb et al. (2012) studied the outflow of normal star-forming galaxies at z=1-2 by using various interstellar absorption lines including those detected in this work. They

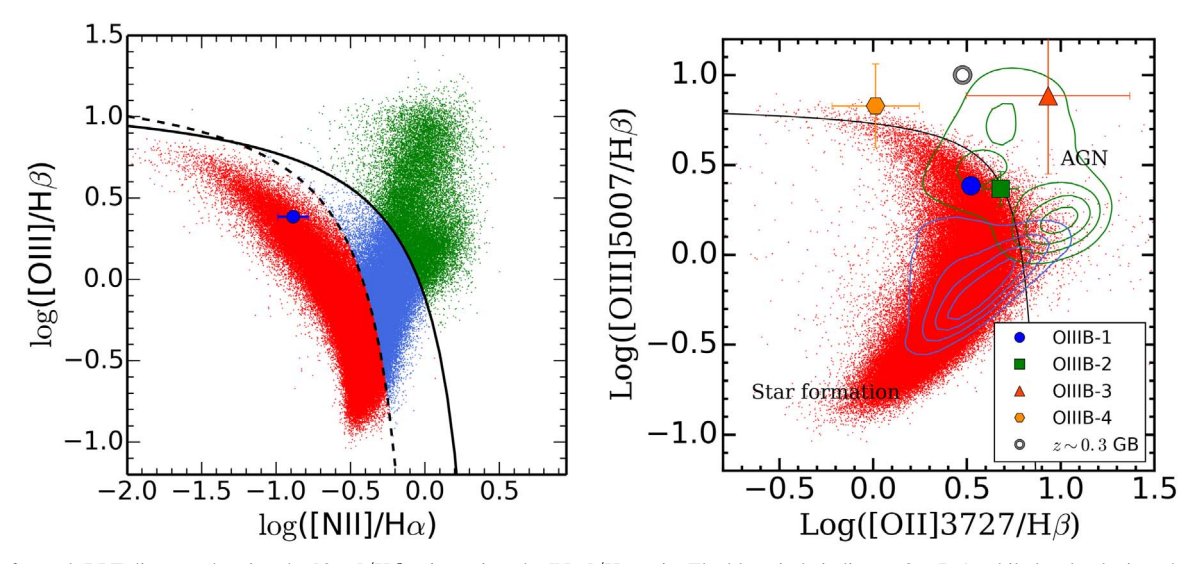


Figure 4. Left panel: BPT diagram showing the  $[O III]/H\beta$  ratio against the  $[N II]/H\alpha$  ratio. The blue circle indicates O IIIB-1, while local galaxies taken from SDSS DR7 data are shown in three different colors. The red, blue, and green dots are for star-forming galaxies, composites, and AGNs, respectively. The black dashed and solid curves are the criteria for separating pure star-forming galaxies, composites, and AGNs by Kauffmann et al. (2003) and Kewley et al. (2001), respectively. Right panel:  $[O III]/H\beta$  vs.  $[O II]/H\beta$  vs.  $[O II]/H\beta$  or the blue diagram of four [O III] blobs at z=0.63 and z=0.83. The line ratios are already corrected for dust attenuation. The blue circle is O IIIB-1 and the green square is O IIIB-2 at  $z\sim0.63$ . O IIIB-3 and O IIIB-4 at  $z\sim0.83$  are indicated with the red triangle and the orange hexagon, respectively. Red dots represent the local star-forming galaxies classified by the BPT diagram in the left panel. Blue and green contours show the distribution of composites and AGNs, respectively. The open gray circle shows a Seyfert type 2 AGN (J2240–0927) at  $z\sim0.3$  with a spatially extended [O III] emission line, which is called a Green Bean (GB; Schirmer et al. 2013). The black solid line divides the blue diagram into two regions of star formation and AGN (Lamareille 2010).

found that the velocity offsets of the Fe II  $\lambda 2600$  and Mg II  $\lambda 2804$  absorption lines of star-forming galaxies at z=1-2 with stellar masses and SFRs comparable to those of O IIIB-1 range between -190 and -130 km s<sup>-1</sup>. The Fe II\* and Mg II lines of O IIIB-1 show velocity offsets slightly higher than those of the normal star-forming galaxies.

### 4.4. AGN Diagnostics

An AGN is one of the plausible energy sources providing hard ionizing photons that can cause the emission lines at large scale. Yuma et al. (2017) carried out a primary check for the AGN contribution in the [O III] blobs by cross-matching the X-ray and radio catalogs obtained by Ueda et al. (2008) and Simpson et al. (2012), respectively. They found no X-ray or radio counterpart for any [O III] blobs in our sample down to the X-ray luminosity of  $10^{42}$  erg s $^{-1}$  as mentioned in Section 2. This luminosity limit is  $\sim\!0.5$  dex brighter than the faintest bin of the X-ray luminosity functions of AGNs at similar redshifts (e.g., Fotopoulou et al. 2016; Ranalli et al. 2016). Thus, we know that the [O III] blobs are not unobscured AGNs, but the possibility that the [O III] blobs are faint or heavily obscured AGNs cannot yet be ruled out.

To further investigate AGN signature in the targets, we first plot the Baldwin, Phillips, and Terlevich (BPT) diagram in the left panel of Figure 4. The BPT diagram is a plot of the [O III]/  $H\beta$  ratio versus the [N II]/ $H\alpha$  ratio (Baldwin et al. 1981). Kewley et al. (2006) used this diagram to efficiently classify their sample into the star-forming galaxies, composites, and AGNs. Compared with star-forming galaxies, AGNs have a higher ionization state, resulting in higher values of both [O III]/ $H\beta$  and [N II]/ $H\alpha$  ratios. We plot local galaxies (z=0.04-0.10) obtained from the Sloan Digital Sky Survey (SDSS) Data Release 7 (DR7; Abazajian et al. 2009) in the left panel of the figure and separate them into pure star-forming galaxies (red), composites (blue), and AGNs (green) based on their locations on the BPT diagram. O IIIB-1 is the only object

that has the NIR spectrum available. It is clearly seen from the figure that O IIIB-1 lies exactly on the distribution of the local star-forming galaxies, indicating that it is a normal star-forming galaxy.

For the remaining three [O III] blobs, we use the blue diagram, which is a plot between the dust-corrected  $[O III]/H\beta$ and  $[O II]/H\beta$  emission line ratios (right panel of Figure 4). AGNs can be distinguished from the star-forming galaxies with the solid curve shown in the right panel of Figure 4 (e.g., Lamareille 2010; Harikane et al. 2014). On the blue diagram, we display the local SDSS galaxies that we already categorized into star-forming galaxies, composites, and AGNs based on the BPT diagram as a reference. The local star-forming galaxies and composites are largely overlapped with each other in the region below the curve that is used to separate the star formation activity from AGNs. On the other hand, AGNs can be distinguished from the star formation galaxies and composites efficiently. Lamareille (2010) stated that the contamination of AGNs in the region of star-forming galaxies on the blue diagram is roughly 16%. We also plot a Seyfert type 2 AGN (J2240–0927) at z = 0.326 that shows the extended [O III] emission line (Schirmer et al. 2013). We discuss the similarity and difference between our [O III] blobs and this AGN in Section 4.7.

From the blue diagram in the right panel of Figure 4, O IIIB-1 is still confirmed to be in the pure star formation region consistent with its location on the BPT diagram. O IIIB-2, on the other hand, shows the higher [O II]/H $\beta$  ratio and get closer to the separation curve. Thus, we cannot rule out the possibility that O IIIB-2 might be fueled by an AGN activity. The other two [O III] blobs at  $z \sim 0.83$  show the remarkably high [O III]/H $\beta$  ratios. O IIIB-3 is clearly located in the AGN region. This is in good agreement with its emission-line width mentioned in Section 4.2. The [O III]  $\lambda$ 5007 line width of 419.5 km s<sup>-1</sup> suggests that O IIIB-3 is plausibly the type 2 Seyfert, whose typical line widths are roughly  $\sim$ 500 km s<sup>-1</sup>.

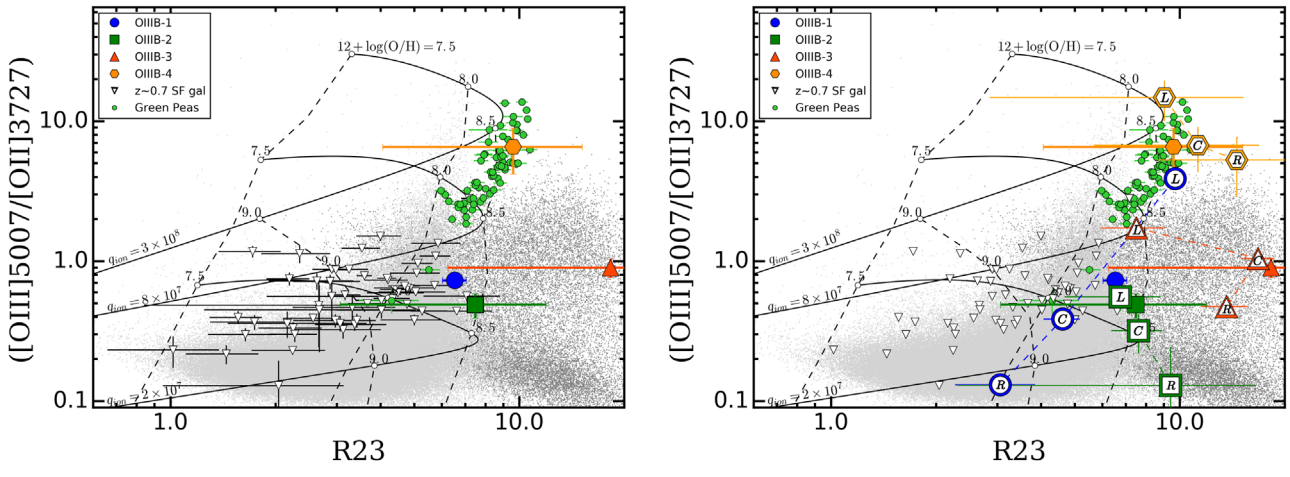


Figure 5. Relation between [O III]/[O II] ratio and R23 index. Left panel: colored symbols represent O IIIBs at  $z\sim0.7$  as in previous figures. Light-gray and darkgray dots are the SDSS star-forming galaxies and AGNs, respectively. Open triangles represent star-forming galaxies at z=0.5–0.9 by Lilly et al. (2003). Green circles are for the local GPs with the strong [O III] emission line by Cardamone et al. (2009). Each solid black line shows a track of photoionization models at constant ionization parameters of  $q_{\rm ion}=2\times10^7$  cm s<sup>-1</sup>,  $8\times10^7$  cm s<sup>-1</sup>, and  $3\times10^8$  cm s<sup>-1</sup> with  $12+\log({\rm O/H})$  in the range of 7.5–9.0 (Kewley & Dopita 2002). The dashed lines connect the photoionization model tracks at a constant  $12+\log({\rm O/H})$ . Right panel: [O III]/[O II] ratio vs. R23 index of the radial profiles of the [O III] blobs. Open symbols with the letters "L," "C," and "R" refer to the left, central, and right parts of the blobs in Figure 6, respectively (more details in main text). Other symbols and lines are identical to those in the left panel.

O IIIB-4 shows the remarkably high  $[O III]/H\beta$  ratio but low  $[O II]/H\beta$  ratio (right panel of Figure 4). The high ratio of [O III] to  $H\beta$  emission lines places O IIIB-4 above the separated curve in the blue diagram. As seen in the blue diagram, some fraction of the local star-forming galaxies distribute in the same region as O IIIB-4, while AGNs do not. It is likely that O IIIB-4 is one of the star-forming galaxies with the strongest  $[O III]/H\beta$  ratio. In conclusion, with the emission-line diagnostics, we can confirm that O IIIB-1 and O IIIB-4 are star-forming galaxies, whereas O IIIB-3 is an obscured AGN. However, there is no clear conclusion for O IIIB-2; it can be a star-forming galaxy, composite galaxy, or AGN.

### 4.5. Properties of ISM

Nakajima et al. (2013) and Nakajima & Ouchi (2014) show that the diagram between the [O III]/[O II] line ratio and the R23 index is efficient to investigate an ionization parameter and metallicity of a star-forming galaxy simultaneously. The emission-line ratio of an atom at different ionization states, such as the [O III]/[O II] ratio, strongly depends on the ionization parameter of gas,  $q_{\rm ion}$ , which is the ratio of the ionizing photon flux per unit area to the number density of hydrogen atoms. The ionization parameter  $q_{\rm ion}$  corresponds to the dimensionless ionization parameter U as  $U \equiv q_{\rm ion}/c$ , where c is the speed of light (Kewley & Dopita 2002). The R23 index is defined as

$$R23 = \frac{\text{[O II]} \lambda 3727 + \text{[O III]} \lambda \lambda 4959, 5007}{\text{H}\beta}.$$
 (1)

The R23 index is one of the good indicators for estimating metallicities of the galaxies (e.g., Pagel et al. 1979; Kewley & Dopita 2002), although it slightly depends on the ionization parameter.

We plot the [O III]/[O II] ratios of the [O III] blobs against their R23 indices in Figure 5 to investigate the properties of their ISM. The local SDSS star-forming galaxies (gray dots), local SDSS AGNs (dark gray dots), and star-forming galaxies at 0.47 < z < 0.92 (open triangles; Lilly et al. 2003) are also

plotted as a reference. Another population that we plot in the figure as a reference is Green Peas (hereafter GPs). GPs are the compact star-forming galaxies at z = 0.112-0.360 with the strong [O III] emission line with a rest-frame EW up to 1000 Å (Cardamone et al. 2009). The [O III] emission line of GPs falling into the r band makes this type of galaxy look green in the g, r, i composite image. In addition to the observed galaxies at various redshifts, we plot photoionization models at constant ionization parameters of  $q_{\rm ion}=2\times 10^7~{\rm cm~s^{-1}},$   $8\times 10^7~{\rm cm~s^{-1}},$  and  $3\times 10^8~{\rm cm~s^{-1}}$  with varying metallicities. The models with the constant metallicities are linked with dashed lines, and the values of the metallicities in terms of  $12 + \log(O/H)$  are indicated by the open circles. The local SDSS star-forming galaxies show a variety of R23 indices ranging from 1.0 to 10.0, while their [O III]/[O II] ratios are mostly below 1.0. Likewise, star-forming galaxies at  $z \sim 0.7$ are distributed in the same area on the plot. It is indicated that most of the star-forming galaxies at z=0 and  $z\sim 0.7$  have ionization parameters between  $q_{\rm ion}=2\times 10^7\,{\rm cm\,s}^{-1}$  and  $q_{\rm ion}=8\times 10^7\,{\rm cm\,s}^{-1}$  but have wide ranges of metallicities. On the other hand, the star-forming GPs with the strong [O III] emission line show high [O III]/[O II] ratios and R23 indices. According to the figure, the GPs at z = 0.1–0.4 show ionization parameters higher than  $8 \times 10^7 \,\mathrm{cm \, s}^{-1}$ , which is clearly higher than the normal star-forming galaxies at z = 0and z = 0.7. Due to the strong [O II] and [O III] emission, the SDSS AGNs at  $z \sim 0$  show high R23 indices that are relatively greater than those of the star-forming galaxies at z = 0 and  $z \sim 0.7$ . Meanwhile, the [O III]/[O II] line ratios of the local AGNs are distributed in the same range as those of the starforming galaxies.

O IIIB-1 and O IIIB-2 are located in the same region as the local and z=0.7 star-forming galaxies, suggesting similar ionization parameters and metallicities. O IIIB-1 and O IIIB-2 should have an ionization parameter slightly less than  $q_{\rm ion}=8\times10^7\,{\rm cm\,s}^{-1}$ . Note that the inferred ionization parameter and metallicities of O IIIB-2 only apply if it is a star-forming galaxy. O IIIB-3 shows huge error bars in the R23 index owing to the low S/N of the H $\beta$  emission line. As O IIIB-

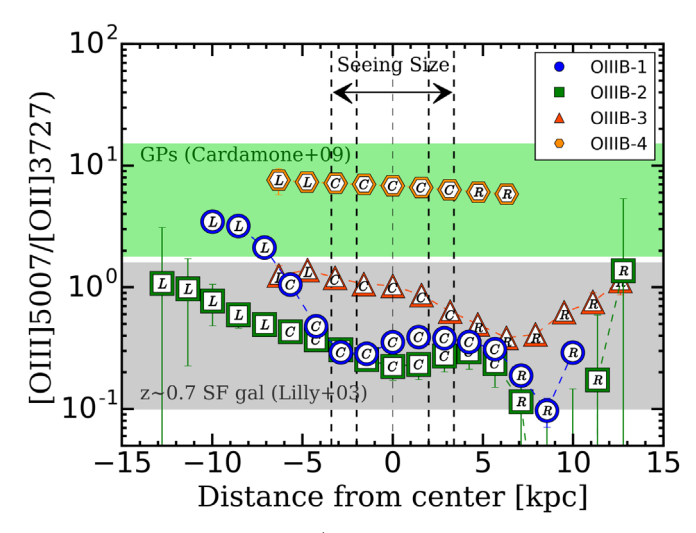


**Figure 6.** Radial profiles of [O III]/[O II] ratios of four O IIIBs at  $z\sim0.7$  as a function of the distance from the center of the blobs. The left-to-right radial profile is drawn from the top to the bottom part of the 2D spectrum in Figure 2. The symbols of the four [O III] blobs are identical to the previous figures. The letters "L," "C," and "R" indicate the regions that we use to determine the left, central, and right components of a given blob, respectively. The gray area represents the typical line ratios of star-forming galaxies at 0.47 < z < 0.92 (Lilly et al. 2003). The green region indicates the line ratios of the GPs at z=0.112-0.360 by Cardamone et al. (2009). The average seeing size of the data is also shown in the figure.

3 is classified as an AGN in Section 4.4, it is obvious that its location is consistent with the AGNs found in the local universe. In contrast, O IIIB-4 is located in a totally different region in Figure 5. O IIIB-4 shows an impressively high [O III]/[O II] ratio, indicating that the ionization parameter  $q_{\rm ion}$  should be roughly  $3 \times 10^8 \, {\rm cm \, s^{-1}}$ . This high [O III]/[O II] ratio of O IIIB-4 agrees well with those of the GPs at z=0.1–0.4.

### 4.6. Radial Profile of the [O III] Blobs

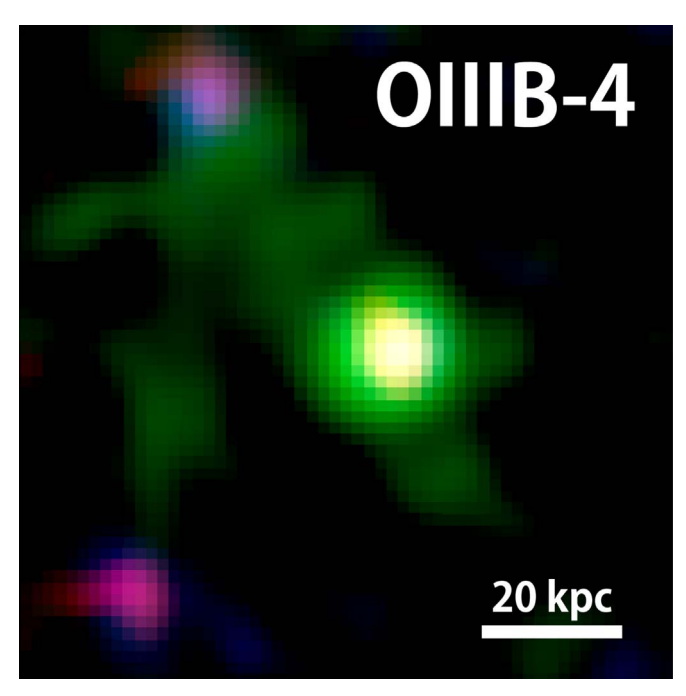
We further investigate the nature of the [O III] blobs by plotting their [O III]/[O II] line ratios as a function of the distance from the center of the blobs. By observing the [O III] blobs with the slits finely aligned along the most extended direction of the [O III] emission line (see Figure 1), we are able to examine the spectroscopic properties of the outer region of the [O III] blobs. The radial profile of the emission line is constructed from the background-subtracted 2D spectrum by integrating the emission line at each spatial position along the wavelength direction covering the full wavelength range of the best-fitted Gaussian profile. This wavelength range covers all spatial components of the emission line. The stellar continuum profiles at the wavelengths blueward and redward of each emission line for a given blob are estimated by creating the continuum profiles using an identical wavelength range as used to create the emission-line profile. Then, we interpolate both continuum profiles to obtain the average continuum profile at the wavelength of the emission line. In this way, we can ensure that the emission-line profile is not over- or underestimated. The spatial profile of the [O III]/[O II] ratio is obtained after carefully removing the estimated stellar continuum and shown in Figure 6. The negative values of the distance from the center refer to the component at the top of the 2D spectral image in

Figure 2. For comparison purposes, we show the shaded regions where the GPs at z = 0.1–0.4 and star-forming galaxies at  $z \sim 0.7$  are typically located.

It is seen from Figure 6 that all four of our samples extend beyond the seeing size of the spectral images. The centers of O IIIB-1, O IIIB-2, and O IIIB-3 lie in the region where the typical star-forming galaxies at  $z \sim 0.7$  are located. Interestingly, the left part of the O IIIB-1 profile at a distance larger than 5 kpc shows the high [O III]/[O II] ratio consistent with the GPs at z = 0.1 - 0.4. Similarly, the [O III]/[O II] ratio of O IIIB-2 increases as a function of the distance from the center on both sides, albeit with a large uncertainty. O IIIB-3 shows an [O III]/ [O II] ratio of roughly 1-2, which is slightly higher than the central parts of O IIIB-1 and O IIIB-2, but it is still in the range of the typical star-forming galaxies. Finally, the [O III]/[O II] radial profile of O IIIB-4 seems to be almost constant at roughly [O III]/[O II] = 5-10 over  $\sim 14$  kpc. It is noteworthy that the spatial extension of O IIIB-4 is smaller than the other three blobs because the slit direction is unfortunately not designed to observe the longest axis of O IIIB-4. The [O III]/[O II] ratios are significantly greater than those of the typical star-forming galaxies and consistent with those of the compact GPs at z = 0.1-0.4. This is in agreement with what we have found in Section 4.5 (left panel of Figure 5), that O IIIB-4 has both [O III]/[O II] ratio and R23 index comparable to those of the GPs. In contrast to O IIIB-4, the GPs show compact morphology in g, r, i images, suggesting that they have a compact stellar component (Cardamone et al. 2009). Although there is no detailed study about the extension of the [O III] emission line of the GPs yet, the compact size of the GPs seen in the rband image, in which the [O III] emission line falls, may imply the compact size of the [O III] emission line as well. The unresolved morphology of the GPs in the r-band image suggested that the sizes of the [O III] emission line should be less than 5 kpc (Cardamone et al. 2009). Further study of the spatial extension of the [O III] emission line for the GPs is necessary to confirm the above statement. The fact that O IIIB-4 shows an extended profile of the [O III] emission line over  $\sim$ 14 kpc makes O IIIB-4 different in size from the GPs at z = 0.1–0.4. Thus, we call O IIIB-4 a giant GP, as it shows a high [O III]/[O II] ratio like the GPs and its spatially extended feature of the [O III] emission line.

We replot the diagram of the [O III]/[O II] ratio against the R23 index in the right panel of Figure 5 by separating the radial profiles of each [O III] blob into three components: the central part and two outer regions on both sides of the profile beyond the stellar continuum. We use letters "L," "C," and "R" to represent the left, central, and right components of each blob, respectively. The left component corresponds to the left part of the radial profile shown in Figure 6. The central component is roughly twice the FWHM of the continuum radial profile to ensure that the extended parts are not contaminated by the stellar contribution. As seen in the figure, the left and central components of O IIIB-2 are close to the plot of the entire object and are located in the region where the star-forming galaxies at  $z \sim 0$  and  $z \sim 0.7$  are distributed. The line ratio of the right subregion of O IIIB-2, however, shows higher R23 index and agrees well with the line ratios of the local SDSS AGNs. Originally, O IIIB-3 shows the high R23 index with a large uncertainty. When we divide O IIIB-3 into three components, the extended parts of O IIIB-3 show slightly lower R23 indices but are still consistent within the large uncertainties. The left

<sup>&</sup>lt;sup>6</sup> This is not the case for O IIIB-2 and O IIIB-4, whose slit direction is fixed to that of O IIIB-3, the brightest [O III] blob in the same mask (see Section 3.1).



**Figure 7.** Composite images of O IIIB-4. North is up, east is left. The red and blue colors of both images are the images observed in the R and z bands, respectively, whereas the green color represents the [O III] emission line observed in the NB921 image. The size of each image is roughly  $12 \times 12$  arcsec², which corresponds to the physical dimension of  $90 \times 90$  kpc² at z = 0.8379. The white bar in the lower right corner indicates the physical scale of 20 kpc.

part of O IIIB-3 falls closer to the GP region, with the [O III]/ [O II] ratio higher than that of the central part, which is in agreement with Figure 6. Meanwhile, the central and right subregions are located close to the integrated line ratio.

For O IIIB-1, the left component moves apart from the rest and falls into the GP region of the high [O III]/[O II] ratios and R23 indices. It can be argued that the extended component of O IIIB-1 has not only a comparable [O III]/[O II] line ratio to the GPs, as seen in Figure 6, but also a similar R23 index. Likewise, the locations of all three components of O IIIB-4 on the [O III]/[O II]-R23 diagram are consistent with those of the GPs. In conclusion, one extended part of O IIIB-1 and the entire O IIIB-4 show [O III]/[O II] ratios and R23 indices consistent with those of the compact GPs at z=0.1-0.4.

## 4.7. Discovery of a Giant Green Pea at z = 0.838

We discover a giant GP, O IIIB-4, which has spatially extended [O III] emission and line ratios consistent with those of the GPs found at z=0.1–0.4 by Cardamone et al. (2009). Figure 7 shows the close-up RGB image of O IIIB-4. The extended green color on the order of 10–20 kpc around the center of O IIIB-4 clearly indicates the large-scale extension of the [O III] emission line. It is noteworthy that the green components in the northeast (top left) direction of O IIIB-4 are also parts of O IIIB-4 when we measure the [O III] surface brightness down to  $1.2 \times 10^{-18} \, \mathrm{erg \, s^{-1} \, cm^{-2} \, arcsec^{-2}}$  (see Figure 1).

The left panel of Figure 8 shows the relation between the rest-frame [O III] EWs of the [O III] blobs and the SFRs derived by using the SED fitting method. In Yuma et al. (2017), the observed SEDs of the [O III] blobs are collected from the photometry in nine bands: BVRizJHK, IRAC ch1 (3.6  $\mu$ m), and

IRAC ch2  $(4.5 \mu m)$ . The magnitudes in the i or z band are excluded because they might be contaminated by the strong [O III] emission line at z = 0.63 or z = 0.83, respectively. The stellar population models are constructed with the Bruzual & Charlot (2003) code by assuming a constant star formation history, a Salpeter (1955) initial mass function with mass cutoffs of 0.1 and  $100 M_{\odot}$ , Calzetti et al. (2000) dust attenuation, and solar metallicity. The effect of varying the parameters used to construct the models (e.g., the IMF, star formation histories, and metallicity) is included in the uncertainties of the derived stellar properties. The rest-frame [O III] EWs of all [O III] blobs are in the range of 200–1000 Å. The giant GP (O IIIB-4) shows the largest EW of 845  $\pm$  27 Å. We also plot the GPs at z = 0.1-0.4 in the figure for comparison purposes. As mentioned earlier, the GPs are selected as the galaxies with excessive fluxes in the r-band image. Hence, they should show very high rest-frame [O III] EWs by definition. The SFRs of the GPs at z = 0.1–0.4 were derived from the dust-corrected  $H\alpha$  fluxes (Cardamone et al. 2009). From the left panel of Figure 8, the rest-frame [O III] EWs of the GPs are typically in the range of 100–2000 Å. All [O III] blobs studied in this paper show EWs in well agreement with the GPs at z = 0.1–0.4. However, O IIIB-1 and O IIIB-2 have significantly higher SFRs than the GPs, indicating more intense activity of star formation. Meanwhile, the giant GP (O IIIB-4) shows the lower SFR of roughly  $15 M_{\odot} \text{ yr}^{-1}$ , which is consistent with the compact GPs at z = 0.1-0.4.

We plot the radial profile of the rest-frame [O III] EW in the right panel of Figure 8 by dividing the profile into three components based on their distances from the center: left (L), center (C), and right (R). O IIIB-4 shows high [O III] EWs in all components. The left and central parts of O IIIB-4 have [O III] EW in the range of 800–1000 Å, consistent with the EW of the entire blob. They are in the same range as the typical GPs at z = 0.1–0.4. The right component even shows the higher EW, albeit with the large error bar due to the low S/N of the faint continuum. This clearly confirms that O IIIB-4 has [O III] EW high enough to be called a giant GP. Among the remaining three [O III] blobs, O IIIB-3 shows a high [O III] EW comparable to the GPs throughout the entire object. On the other hand, O IIIB-1 and O IIIB-2 show [O III] EWs at the center slightly smaller than those of the typical GPs at z = 0.1–0.4. Their [O III] EWs are on the order of 100 A, while the [O III] EWs of the extended components increase to approximately 150-250 Å in the case of O IIIB-2. The left component of O IIIB-1 shows a significantly large EW of more than 1000 Å. It is consistent with what we have found in the right panel of Figure 5, that the left part of O IIIB-1 has an [O III]/[O II] line ratio and R23 index comparable to those of the GPs.

Besides the GPs at z=0.1–0.4, there is another population that is similar to our giant GP. Schirmer et al. (2013) discovered Seyfert-2 galaxies at  $z\sim0.3$  in SDSS DR8 with luminous narrow-line regions and named these galaxies GBs. GBs show the high [O III] luminosities on the order of  $10^{43}$  erg s<sup>-1</sup> and large [O III]/[O II] ratios of more than 1.0. Compared with GPs at similar redshifts, GBs are much larger, with a size of the [O III] emission line of 15–20 kpc, and show higher [O III]/[O II] ratios. Their [O III] EWs are on the order of 1000 Å. GBs at  $z\sim0.3$  are similar to O IIIB-4 in terms of the

<sup>&</sup>lt;sup>7</sup> IRAC ch1 and ch2 are the mid-infrared data obtained with the Infrared Array Camera from the *Spitzer* UKIDSS Ultra Deep Survey (SpUDS; PI: J. Dunlop).

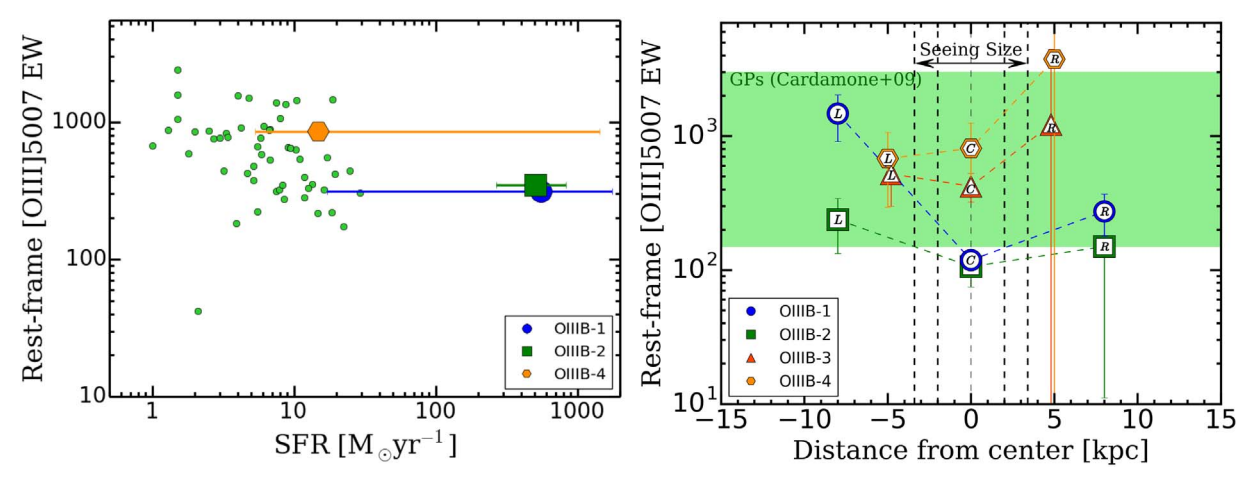


Figure 8. Left panel: relation between the rest-frame [O III] EWs ([O III] EWs) and the SFRs of four [O III] blobs at  $z \sim 0.63$  and  $z \sim 0.83$ . The symbols of the [O III] blobs are identical to those in the previous figures. The small green circles show the GPs discovered at z = 0.1–0.4 by Cardamone et al. (2009). Right panel: rest-frame [O III] EWs of the [O III] blobs as a function of the distance from the center. The radial profile of each [O III] blob is divided into three components: left (L), center (C), and right (R), corresponding to the left, center, and right parts of the profile shown in Figure 6.

large [O III] EW and the spatial extension of the [O III] emission line. However, the [O III]/[O II] ratios of GBs are slightly higher than those of O IIIB-4. The main difference between O IIIB-4 and GBs is the energy source; GBs are Seyfert type 2 AGNs, but O IIIB-4 is a star-forming galaxy. We plot the most prominent GB, J2240–0927, in the right panel of Figure 4. Its location on the blue diagram is consistent with the distribution of local SDSS AGNs, whereas O IIIB-4 is located close to the local star-forming galaxies on the same figure. Additionally, the high-ionization lines such as [Ne V] emission are not detected in O IIIB-4. The  $3\sigma$  flux limit for nondetection is roughly  $1.0 \times 10^{-18} \, {\rm erg \, s^{-1} \, cm^{-2}}$ , which provides a  $3\sigma$  upper limit on the [Ne V]/H $\beta$  ratio of O IIIB-4 of <0.03. In contrast, the [Ne V] emission line is detected in many GBs, including J2240–0927, with an [Ne V]/H $\beta$  ratio of 0.22 (Schirmer et al. 2016).

Figure 9 shows the correlation between the [O III]/[O II] line ratios and four different physical properties: stellar mass  $(M_*)$ , SFR, sSFR (=SFR/ $M_*$ ), and  $\mu_{0.32}$ . The stellar mass and SFR of the [O III] blobs are derived by the SED fitting method (Yuma et al. 2017).  $\mu_{0.32}$  is defined as a combination of  $M_*$  and the SFR proposed by Mannucci et al. (2010):

$$\mu_{\alpha} = \log_{10}(M_*) - \alpha \log_{10}(SFR), \tag{2}$$

where  $\alpha=0.32$  provides the minimum scatter of the SDSS galaxies in the local universe in the  $\mu_{\alpha}$ -metallicity plane. The metallicity in terms of  $12 + \log({\rm O/H})$  can be empirically estimated from  $\mu_{0.32}$  as

$$12 + \log(O/H) = 8.90 + 0.39x - 0.20x^{2} - 0.077x^{3} + 0.064x^{4},$$
 (3)

where  $x=\mu_{0.32}-10$  (Mannucci et al. 2010). It is noteworthy that Equation (3) is obtained by fitting the local SDSS galaxies with stellar masses of  $\log(M_*)=9$ –11  $M_\odot$  or  $\mu_{0.32}$  in the range of  $\mu_{0.32}=9.0$ –11.5. In this fitting range, the metallicity 12 +log(O/H) decreases with  $\mu_{0.32}$ . We would reach the minimum metallicity of 12+log(O/H) = 8.4 at  $\mu_{0.32}=8.73$ . This relation might not be highly accurate for galaxies with

 $\mu_{0.32}$  smaller than 8.73. However, it seems that the metallicity continues to decrease at  $\mu_{0.32}$  below 8.73 but becomes constant at  $\mu_{0.32}$  greater than 10.5. Mannucci et al. (2010) also proposed that the metallicity of star-forming galaxies with any stellar mass, any SFR, and at any redshift up to z=2.5 practically follows the linear correlation between  $12 + \log(O/H)$  and  $\mu_{0.32}$ :

$$12 + \log(O/H) = 8.90 + 0.47x$$
 if  $\mu_{0.32} < 10.2$ , (4)

where  $x = \mu_{0.32}$ -10. Therefore,  $\mu_{0.32}$  can basically represent the metallicity of the galaxies with a stellar mass in the range of  $\log(M_*) = 9$ -11  $M_{\odot}$ .

As mentioned earlier, the giant GP, O IIIB-4, shows the highest [O III]/[O II] ratio among all four [O III] blobs discussed in this paper. It is located in different locations from the rest of the [O III] blobs in all plots in Figure 9. The stellar mass of O IIIB-4 is  $6.75^{+11.22}_{-2.91} \times 10^7 \, M_{\odot}$ . Compared with the other [O III] blobs in our sample, O IIIB-4 is the [O III] blob with the smallest  $M_*$  and the lowest  $\mu_{0.32}$ . The sSFR of O IIIB-4 is  $\sim 2 \times 10^2 \, \text{Gyr}^{-1}$ , which is comparable to the other [O III] blobs. In fact, most of the [O III] blobs found at z = 0.63 and z = 0.83 show a high sSFR that is greater than the sSFR of typical star-forming galaxies on the so-called main sequence of the stellar mass-SFR diagram (Elbaz et al. 2007; Yuma et al. 2017). O IIIB-4 is the [O III] blob at  $z \sim 0.83$  with the smallest stellar mass. Even if we compare O IIIB-4 with the normal [O III] emitters at the same redshift, we would still find that O IIIB-4 is among the emitters with the smallest stellar mass and highest sSFR (see Figures 12 and 13 in Yuma et al. 2017). The high [O III]/[O II] line ratio of O IIIB-4 is comparable to the z = 0.1-0.4 GPs; however, their stellar properties are not exactly consistent. O IIIB-4 has a stellar mass smaller than a majority of the GPs and SDSS galaxies. The sSFR of O IIIB-4 is consistent with two GPs at z = 0.1-0.4, while it is higher than those of the remaining GPs. The low  $\mu_{0.32}$  of O IIIB-4, as seen in the bottom right panel of Figure 9, may imply its low metallicity. Amorín et al. (2010) showed that the GPs at z = 0.1 - 0.4have metallicities in the range  $7.6 < 12 + \log(O/H) < 8.4$ . The comparable line ratios between O IIIB-4 and the GPs may imply that the metallicity of O IIIB-4 is likely similar to that of the GPs. The implied

 $<sup>^8</sup>$  Note that we do not plot O  $\rm IIIB\text{-}3$  in Figure 9 because the AGN contribution might affect the SED fitting results.

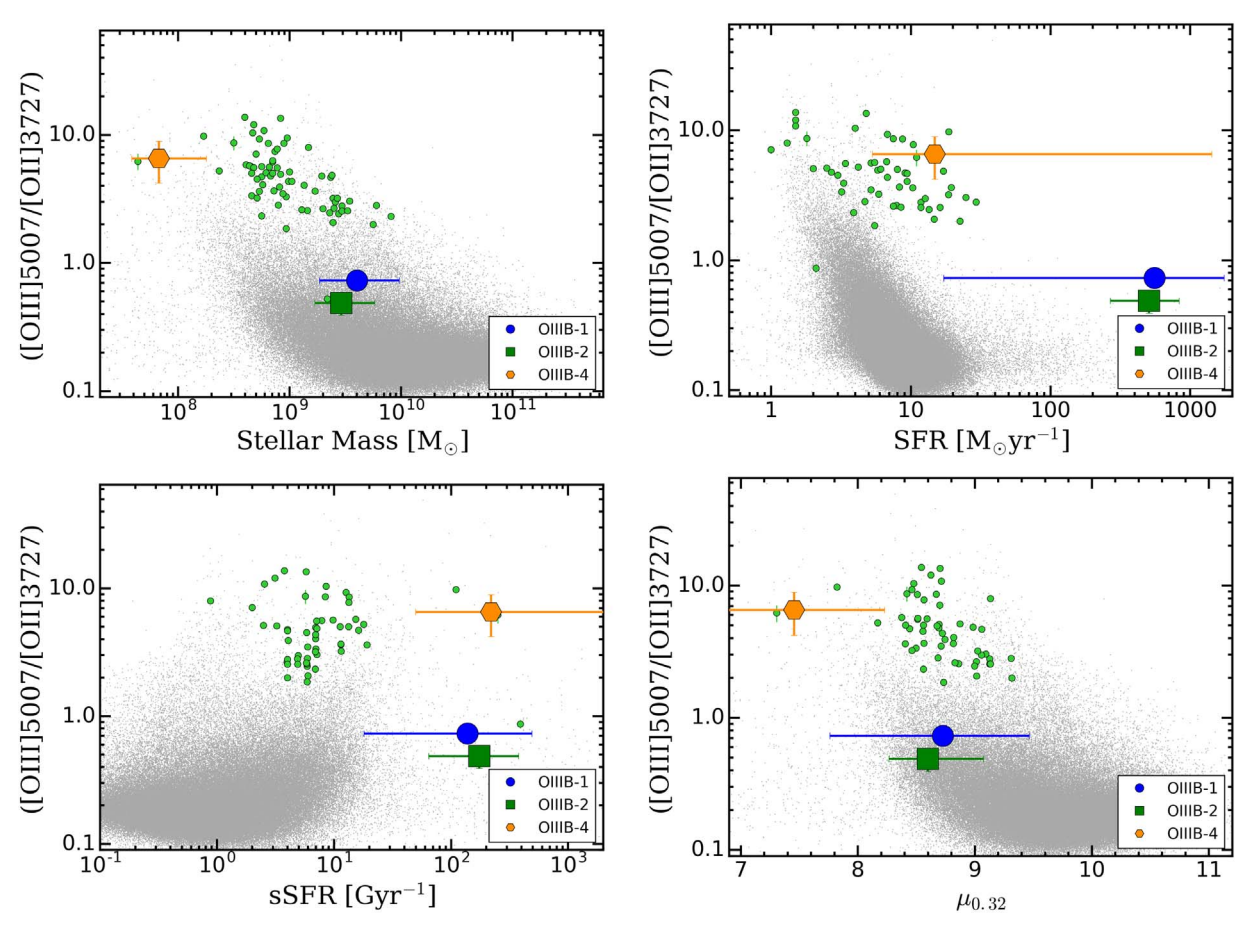


Figure 9. Diagrams of the [O III]/[O II] ratios vs. the stellar mass  $(M_*; top left)$ , SFR (top right), sSFR (bottom left), and  $\mu_{0.32}$  (defined by Mannucci et al. 2010; bottom right). Symbols are identical to those in the previous figures.

subsolar metallicity of O IIIB-4 might affect the stellar properties derived by the SED fitting method in that the models with subsolar metallicity give slightly lower SFRs (0.12 dex) than those with solar metallicity (Yabe et al. 2009). However, the effect of varying metallicity of models is already included in the uncertainties of the derived properties.

With the small stellar mass and low metallicity, O IIIB-4 is somehow similar to the galaxies with extreme emission lines at low redshifts (e.g., Amorín et al. 2014; Izotov et al. 2017; Yang et al. 2017). Amorín et al. (2014) found the galaxies at  $0.2 \leqslant z \leqslant 0.9$  with high rest-frame [O III] EWs of 100-1700 Å. They also suggested high-ionization parameters of  $q \ge 10^8 \,\mathrm{cm \, s^{-1}}$ , sSFR of 1–100 Gyr<sup>-1</sup>, and metallicity of  $7.5 < 12 + \log(O/H) < 8.3$ , which are similar to OIIIB-4. Amorin et al. (2014) also determined the  $\mu_{0.32}$  of their sample to be in the range of  $\mu_{0.32} = 7.0-8.5$ . This is also consistent with the  $\mu_{0.32}$  of O IIIB-4. Izotov et al. (2017) and Yang et al. (2017) conducted separate surveys and found the galaxies with extreme [O III]/[O II] emission-line ratios at z < 0.07 and z < 0.05, respectively. Yang et al. (2017) proposed the photometric method to select these galaxies and called them the blueberry galaxies, which are basically GPs with low masses. The blueberry galaxies show low stellar masses and high [O III]/[O II] ratios comparable to those of O IIIB-4. However, the only obvious difference between O IIIB-4 and these extreme emission-line galaxies is the physical size of the emission line. These galaxies show a size so compact that some of them are unresolved in the SDSS images (Yang et al. 2017).

The average properties of O IIIB-1 are indistinguishable from those of O IIIB-2; it is located close to O IIIB-2 in all plots in Figure 9. Although the [O II]/[O II] line ratios of O IIIB-1 and O IIIB-2 are not as high as those of O IIIB-4 and GPs, they are still somewhat higher than the majority of the local starforming galaxies. According to the figure, O IIIB-1 and O IIIB-2 show moderate masses of roughly  $(3-5) \times 10^9 M_{\odot}$ , significantly high SFR on the order of a few hundred  $M_{\odot}$  yr<sup>-1</sup>, and subsequently high sSFR as compared with the local starforming galaxies. Their  $\mu_{0.32}$  values are less than most starforming galaxies in the local universe, implying metallicities lower than those of the local star-forming galaxies.

### 5. Discussion

We know from Section 4.4 that AGN activity is possibly responsible for the spatial extension of the [O III] emission line in only one blob, O IIIB-3, but we cannot make a constraint on the AGN contribution of O IIIB-2. O IIIB-2 can be a star-forming galaxy, composite, or AGN. Thus, we do not further discuss the origins of O IIIB-2 and O IIIB-3 because of the possible AGN contribution. The giant GP (O IIIB-4) with the remarkably high [O III]/[O II] line ratios and O IIIB-1 are likely to be heated by the star formation activity with the high sSFR. Jaskot & Oey (2013) studied six most extreme GPs at z = 0.1–0.4 with the highest [O III]/[O II] ratios. They examined possible origins of the He II  $\lambda$ 4686 emission detected in most of their sample, including Wolf-Rayet stars, AGNs, and fast radiative shocks. Because of the size difference of the

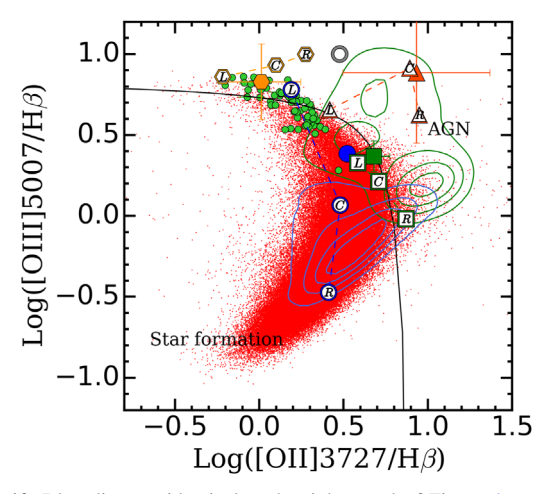


**Figure 10.** Blue diagram identical to the right panel of Figure 4, overplotted with three spatial components of the [O III] blobs. The letters "L," "C," and "R" correspond to the left, center, and right components of each blob, respectively. The circle, square, hexagon, and triangle represent O IIIB-1, O IIIB-2, O IIIB-3, and O IIIB-4, respectively. Small green circles are the GPs at z=0.112-0.360 by Cardamone et al. (2009). Red dots are the local SDSS star-forming galaxies. Blue and green contours represent composites and AGNs, respectively.

[O III] emission lines between the GPs at z=0.1–0.4 and [O III] blobs at  $z\sim0.7$ , the physical structures in the extended regions of the [O III] blobs may be different from the GPs. In this section, we discuss plausible scenarios and physical conditions that maybe able to explain the extended [O III] emission in O IIIB-1 and O IIIB-4, including an AGN light echo (e.g., Schawinski et al. 2015; Ichikawa et al. 2019), fast radiative shocks (e.g., Kewley et al. 2001; Allen et al. 2008; Shirazi & Brinchmann 2012), and the density-bounded system (e.g., Nakajima et al. 2013; Nakajima & Ouchi 2014).

### 5.1. AGN Light Echo

An AGN plays an important role in regulating the galaxy evolution. The accretion to the supermassive black hole at the center of the AGN produces a significant amount of radiative energy that is able to photoionize the ISM of the host galaxy and cause large-scale gas outflows from the host galaxy (e.g., Silk & Rees 1998). In this mode of the AGN activity, AGN photoionization overcomes the photoionization from the HII region of the host galaxy, so the host galaxy can be identified as an AGN (e.g., Baldwin et al. 1981; Veilleux & Osterbrock 1987; Lamareille 2010). It has been long known that an AGN can show luminosity variability (Ulrich et al. 1997). It is possible that the AGN photoionization occurs after the accretion stops because the light echo from the past AGN activity takes time to travel across the ISM of the host galaxy (e.g., Schawinski et al. 2015). In this period of the AGN light echo, an AGN signature such as the X-ray emission at the center of the galaxy is not visible, but we can still observe the extended emission of the galaxy. Although O IIIB-4 and O IIIB-1 do not show any signature of the current AGN activity, it is still possible that their extended emission lines are the effect of the past AGN activity. If this is the case, O IIIB-4 and O IIIB-1 should show AGN-like line ratios in the extended components.

We plot the blue diagram again in Figure 10, but this time we separate the line ratios into three components based on the distance from the center of the [O III] blob (see also Section 4.6). For comparison purposes, we also plot the line ratios of the GPs at z=0.1–0.4. All components of O IIIB-4

show  $[O III]/H\beta$  ratios consistent with the GPs and some fraction of the local star-forming galaxies that show high  $[O III]/H\beta$  ratios. For O IIIB-1, the left component with the high [O III]/[O II] ratio seen in the right panel of Figure 5 and in Figure 6 is located in the GP region. Therefore, it is unlikely that the extended [O III] emission lines of O IIIB-4 and O IIIB-1 are caused by the AGN photoionization left as the AGN light echo after the supermassive black hole at the center stops accreting. It is also seen from the figure that all components of O IIIB-2 lie in the intersect region of star-forming galaxies, composites, and AGNs. The line ratios of the central and right components of O IIIB-3 are consistent with those of AGNs, while the left component shows a lower  $[O II]/H\beta$  ratio, closer to the star-forming galaxies and the GPs.

#### 5.2. Fast Radiative Shock

Without the AGN contribution, the extended [O III] emission line and the gas outflow observed in O IIIB-4 and O IIIB-1 are most likely fueled by the intense star formation activity (see also Section 4.7). However, some physical conditions are still required to explain such high [O III]/[O II] ratios in the extended parts of the [O III] blobs. Supersonic motion of supernovae or gas outflows from a galaxy are able to create the radiative shock with energy high enough to strongly affect the H II region and the ISM of the galaxy. A fast radiative shock, where extreme-ultraviolet and soft X-ray photons are created by strong ionizing radiation behind the shock front, is one of the plausible explanations for the existence of the highly ionized emission lines (e.g., Dopita & Sutherland 1996; Allen et al. 2008).

Allen et al. (2008) developed the library of radiative shock models called "MAPPINGS III," for the ISM with various ranges of metallicities (solar, Small Magellanic Cloud, and Large Magellanic Cloud metallicities), preshock densities of  $0.01-1000 \,\mathrm{cm}^{-3}$ , and shock velocities of  $100-1000 \,\mathrm{km \, s}^{-1}$ . When the velocity of the shock increases, the velocity of the photoionization front increases and exceeds the shock velocities at a certain velocity limit ( $v_{\text{shock}} \approx 170 \, \text{km s}^{-1}$ ). At this point, the photoionization front is separated from the shock front and forms a "precursor" of the HII region, which dominates the optical emission of shocks at high shock velocities (Allen et al. 2008). In the models of shock +precursor, the  $[O III]/H\beta$  ratios become consistent with those of the extended components of the [O III] blobs, i.e.,  $\log(\mathrm{O\,III}]/\mathrm{H}\beta) \geqslant 0.5$  (see Figure 10), when the shock velocity reaches  $v_{\mathrm{shock}} \geqslant 350\,\mathrm{km\,s}^{-1}$  regardless of the values of the magnetic field and the metallicity. The prominent emission lines that are indicative of the fast radiative shocks include He II  $\lambda$ 4686 and [Ne V]  $\lambda\lambda$ 3346, 3426 (e.g., Dopita & Sutherland 1996; Thuan & Izotov 2005; Izotov et al. 2012; Jaskot & Oey 2013). However, we do not detect the He II or [Ne V] emission line in O IIIB-4 and O IIIB-1 above the  $3\sigma$  flux limit of roughly  $1.0 \times 10^{-18} \, \mathrm{erg \, s^{-1} \, cm^{-2}}$ . This places the upper limit of the He II/H $\beta$  ratios at <0.03 in the case of O IIIB-4. O IIIB-1 even seems to show He II  $\lambda 4686$  as an absorption line (left panel of Figure 11). The nondetection of He II and [Ne V] of O IIIB-4 is also shown in the middle and right panels of the figure, respectively. The lowest shock velocity of 100 km s<sup>-1</sup> in the MAPPINGS III shock models by Allen et al. (2008) suggests an He II/H $\beta$  line ratio of 0.47 assuming a density of  $n = 1.0 \,\mathrm{cm}^{-3}$  and solar abundance.

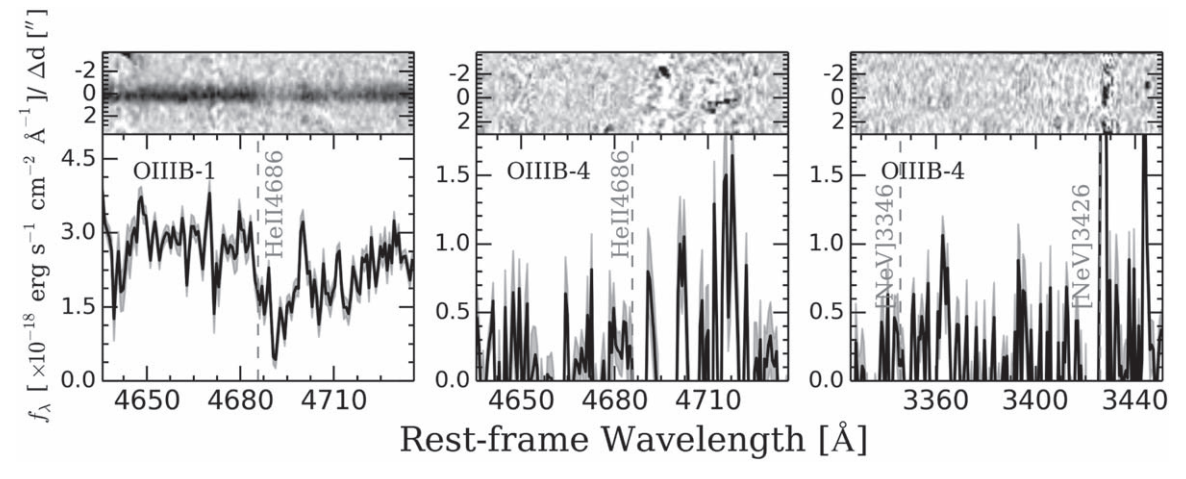


Figure 11. 1D and 2D spectra of O IIIB-1 (left panel) and O IIIB-4 (middle and right panels) at the wavelengths of He II  $\lambda$ 4686 and [Ne V]  $\lambda\lambda$ 3346, 3426. The expected wavelength of each line is indicated with the gray dashed line.

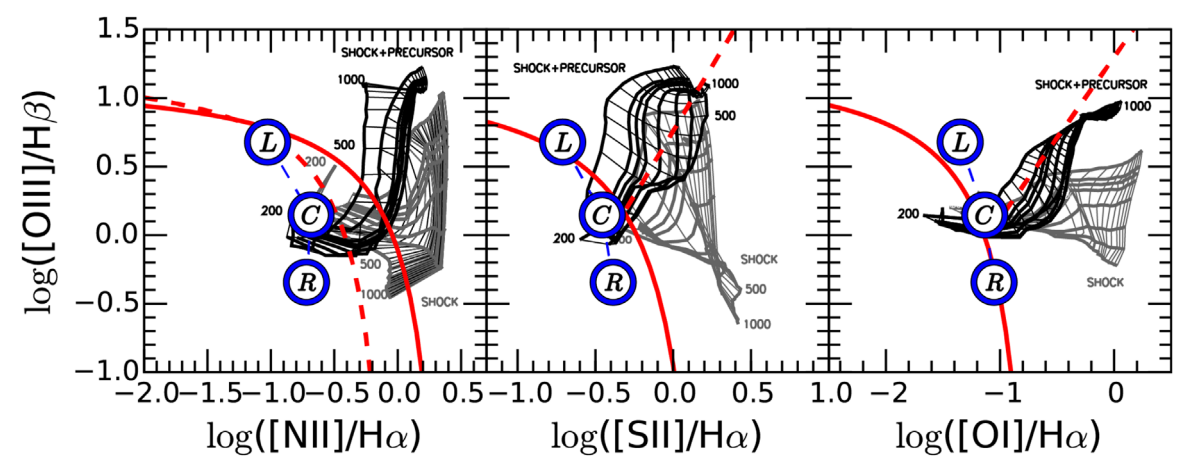


Figure 12. Emission-line diagnostic diagrams of O IIIB-1. Symbols for O IIIB-1 are identical to those in the previous figures. The gray and black grids show the shock-only and shock+precursor models with solar abundance and preshock density of n=1 cm<sup>-3</sup> obtained from MAPPINGS III (Allen et al. 2008), respectively. The grid consists of the lines of constant shock velocity in the range of 200–1000 km s<sup>-1</sup> with 50 km s<sup>-1</sup> intervals (thin lines) and the lines of constant magnetic parameter ranging from  $B/n^{3/2} = 0.0001 \,\mu\text{G cm}^{3/2}$  to  $B/n^{3/2} = 10.0 \,\mu\text{G cm}^{3/2}$  (thick lines).

For O IIIB-1, for which we have Keck/MOSFIRE NIR spectra, we also use another line diagnostics to investigate the shock scenario. Figure 12 shows the line ratios of each component of O IIIB-1 in various emission-line diagnostic diagrams. The grids of both shock-only and shock+precursor models are also illustrated in the figure in the case of solar metallicity and preshock density of  $n=1\,\mathrm{cm}^{-3}$ . It is clearly seen that the left component of O IIIB-1 is not in the shock regions in all diagrams. Therefore, it is unlikely that the fast radiative shock is a physical process responsible for the high-ionization parameters observed in O IIIB-4 and the extended part of O IIIB-1.

# 5.3. Density-bounded Nebulae

As already seen in Figure 5, the  $[O\ III]/[O\ II]$  ratio strongly depends on the ionization parameter and metallicity. The  $[O\ III]/[O\ II]$  ratio increases with increasing ionization parameters and decreasing metallicities. In addition, Shirazi et al. (2014) argued that the high gas density of high-redshift galaxies affects the extreme value of  $[O\ III]/[O\ II]$  ratios. Nakajima & Ouchi (2014) studied the ISM of star-forming galaxies at z=0–3 and found that the  $[O\ III]/[O\ II]$  line ratio also depends on the escape fraction of the ionizing photons,

which is defined as the ratio of ionizing photons escaping the galaxy to the totally produced ionizing photons. To explain the relationship between the [O III]/[O II] ratio and the escape fraction, they classified star-forming nebulae into two types: ionization-bounded and density-bounded nebulae. The size of the ionization-bounded nebulae is equivalent to the Strömgren radius, which is determined by the ionization equilibrium between the producing rate of ionizing photons and the recombination rate. In the ionization-bounded nebulae, the high-ionization state of oxygen ions (producing [O III]) locates close to the ionizing sources, while the envelope of the O<sup>+</sup> ions that produce [O II] is around the edge of the nebulae (e.g., Shields 1990; Oey & Kennicutt 1997; Pellegrini et al. 2012; Nakajima & Ouchi 2014). On the other hand, some fraction of the ionizing photons is allowed to escape from the homogeneous density-bounded nebulae. The HI clouds around the density-bounded nebulae are so small that they are completely ionized. The radius of the density-bounded nebulae is thus constrained by the density of the gas cloud instead of the Strömgren radius, as the complete Strömgen sphere cannot be formed. The size of the O<sup>+</sup> region is thus smaller in the density-bounded nebulae than it is in the ionization-bounded system. With a similar size to the O<sup>2+</sup> region, the densitybounded nebulae would show larger  $[O\,III]/[O\,II]$  ratio in the extended part.

The high [O III]/[O II] ratios of O IIIB-4 may be explained by the hypothesis that the [O III] blob is the density-bounded nebula. The [O III]/[O II] ratio in the outer region is due to the escaping ionizing photons produced by the intense star formation activity at the center of the blob. Arthur et al. (2011) performed a radiation-magnetohydrodynamic (MHD) simulation of the formation and expansion of the H II regions. They showed that the highly ionized density-bounded nebula is strongly influenced by the radiative feedback and gas instability, leading to the peculiar gas morphologies. O IIIB-1 has only one side with a high [O III]/[O II] ratio, implying the asymmetric morphology of the outflow. However, it does not explain why the [O III]/[O II] ratio increases at a greater distance from the center of O IIIB-1. Normally, the [O III]/[O II] ratio should decrease as a function of the distance from the center, as the  $O^+$  ions increase while the  $O^2$  ions decrease at the outer region (Pellegrini et al. 2012). The studies of diffuse ionized gas (DIG) beyond the H II regions of the local galaxies typically show the decrease in [O III]/[O II] ratios at the outer region of the galaxies and suggest lower ionization parameters of DIG than those of the H II regions (e.g., Zhang et al. 2017). The higher [O III]/[O II] ratio of the left component of O IIIB-1 than the rest of the galaxy seems to contradict the typical DIG in the local universe. Nonetheless, Weber et al. (2019) performed a numerical analysis to predict the line ratios of HII regions and DIG by varying the metallicity, stellar effective temperature, and escape fraction  $f_{\rm esc}$ . They found that the [O III]/[O II] ratios increase with radius only in the models of the density-bounded leaky H II regions with a stellar effective temperature of 40,000 K and an escape fraction of less than 10%. This might be the case for O IIIB-1. O IIIB-1 may have the peculiar gas morphology that can cause the leakage of highly ionized photons through a hole in some direction away from the line of sight to the center of the galaxy. Dense gas clouds in the line of sight lead to the low escape fraction, whereas the [O III] emission is largely scattered toward us from the extended region (Bassett et al. 2019). Further constraint on the escape fraction of O IIIB-1 is necessary to confirm this scenario.

### 6. Summary

[O III] blobs are galaxies that exhibit the strong and spatially extended [O III] emission line beyond their stellar continuum. The first systematic survey of [O III] blobs has been conducted by Yuma et al. (2017). In this paper, we investigate the physical nature of the [O III] blobs in more detail by using optical and NIR spectroscopy. We choose the spectroscopic targets based on their large extension of the [O III] emission line and their coordinates to maximize the number of targets per the observed mask. As a result, we observed the two largest [O III] blobs at  $z \sim 0.63$  (O IIIB-1 and O IIIB-2) and another two [O III] blobs at  $z \sim 0.83$  (O IIIB-3 and O IIIB-4) in the optical wavelengths with Subaru/FOCAS. O IIIB-1 was also observed in the NIR wavelength with Keck/MOSFIRE. The main results are listed below.

1. We confirm the spectroscopic redshifts of all targets to be at the expected redshifts, i.e., O IIIB-1 and O IIIB-2 are at z=0.6210 and z=0.6413, respectively. O IIIB-3 and O IIIB-4 are at z=0.8365 and z=0.8379, respectively.

- 2. The original survey of [O III] blobs was based on the hypothesis that the spatially extended [O III] emission line is caused by the large-scale outflow of gas from the center of galaxies. We could confirm the outflow signature in O IIIB-1, which has a stellar continuum bright enough to be detected with the high S/N. The blueshifted Fe II  $\lambda 2326$  absorption, Fe II\*  $\lambda 2626$  fine-structure emission, and Mg II  $\lambda 2804$  absorption lines are detected with the central velocity offsets of -160, -200, and  $-270\,\mathrm{km\,s^{-1}}$ , respectively. The outflow velocities are slightly higher than those of normal star-forming galaxies at z=1-2 by Erb et al. (2012).
- 3. We examine AGN contribution by using the BPT diagram for OIIIB-1 with available NIR data and the  $[O III]/H\beta$  versus  $[O II]/H\beta$  diagram for the other three blobs, of which we have only the optical spectroscopic data. Among the four observed [O III] blobs, O IIIB-3 is the only one that is heated by an AGN activity at the center based on its location on the  $[OIII]/H\beta$  versus  $[O II]/H\beta$  diagram. O IIIB-1, on the other hand, is located in the region consistent with the the pure star formation activity on the BPT diagram. O IIIB-4 is another [O III] blob that is identified as a normal star-forming galaxy in the blue diagram, though it shows a remarkably high [O III]/[O II] line ratio. Lastly, we could not rule out the possibility of AGN contribution in O IIIB-2; it is likely to be a composite powered by both star formation and AGN activities.
- 4. The properties of the ISM surrounding the [O III] blobs have been examined by the [O III]/[O II]–R23 diagram. O IIIB-1, O IIIB-2, and O IIIB-3 show [O III]/[O II] line ratios comparable to those of the local SDSS galaxies and the star-forming galaxies at  $z \sim 0.7$ . Their inferred ionization parameters should be slightly less than  $q_{\rm ion} = 8 \times 10^7 \, {\rm cm \ s^{-1}}$ . Interestingly, O IIIB-4 exhibits an impressively high [O III]/[O II] ratio. The line ratio and the R23 index of O IIIB-4 agree well with those of the compact GPs at z = 0.1–0.4. The ionization parameter of O IIIB-4 should be roughly on the order of  $10^8 \, {\rm cm \ s^{-1}}$ .
- 5. The radial profile of the [O III]/[O II] ratios indicates that O IIIB-4 shows an [O III]/[O II] ratio much greater than those of the star-forming galaxies at  $z \sim 0.7$  and the other three [O III] blobs. The radial profile of O IIIB-4 shows almost constant [O III]/[O II] emission-line ratios of approximately 5–10 over 14 kpc. The [O III]/[O II] ratios are consistent with those of the GPs at z=0.1–0.4; however, the physical sizes are different, as the GPs are compact with [O III] emission lines within 5 kpc. Thus, we call O IIIB-4 a giant GP. Among the remaining three blobs, there is only one extended part of O IIIB-1 showing an [O III]/[O II] ratio as high as the GPs. It is suggested that such a high [O III]/[O II] ratio found in the GPs at z=0.1–0.4 can also be found in the extended component beyond the stellar continuum of the galaxies as well.
- 6. The rest-frame [O III] EW of O IIIB-4 is  $845 \pm 27$  Å. This is well in agreement with the typical GPs at z = 0.1–0.4, which are the galaxies with high [O III] EWs by definition. The [O III] EWs of O IIIB-4 are still consistent with those of the GPs, whose [O III] EWs are in the range of 100–2000 Å, even if we divide the radial profile into three components according to the distance from the center of the blob. O IIIB-1, O IIIB-2, and O IIIB-

3 also have rest-frame [O III] EWs in the same ranges as the GPs. When we divide the EWs into three components, the large [O III] EW of the left component of O IIIB-1 (>1000 Å) is obviously seen. It is in agreement with the [O III]/[O II] ratio and the R23 index of this component, which are similar to those of the GPs. However, the centers of O IIIB-1 and O IIIB-2 show [O III] EWs of  $\sim\!100\,\text{Å}$ , slightly smaller than those of the GPs.

- 7. The giant GP, O IIIB-4, is also similar to GBs at  $z\sim0.3$  in that they show comparable [O III] EWs and consistent spatial extension of the [O III] emission line. However, unlike O IIIB-4, GBs are powered by AGNs rather than star formation.
- 8. The giant GP, O IIIB-4, is the [O III] blob at  $z \sim 0.83$  that has a low stellar mass of  $7 \times 10^7 M_{\odot}$ , a high sSFR of  $2 \times 10^2 \, \mathrm{Gyr}^{-1}$ , and low metallicity. Its physical properties are similar to those of the GPs found at z = 0.1–0.4.
- 9. We check whether or not the [O III] extensions of O IIIB-4 and O IIIB-1 are an AGN light echo influenced by the AGN activities in the past. The blue diagram suggests that the extended parts of O IIIB-4 and O IIIB-1 are caused by the star-forming activity. Thus, we can rule out the AGN light echo scenario.
- 10. The fast radiative shock is another potential mechanism to explain the high [O III]/[O II] ratios. We do not detect the shock-indicative emission lines such as [Ne V]  $\lambda\lambda$ 3346, 3426 and He II  $\lambda$ 4686 in O IIIB-4 and O IIIB-1 at the  $3\sigma$  flux limit of  $1.0\times10^{-18}$  erg s<sup>-1</sup> cm<sup>-2</sup>. The upper limit of the He II/H $\beta$  ratios (<0.03) suggests that the fast radiative shock is unlikely.

The most likely scenario to explain the high [O III]/[O II] ratios observed in O IIIB-4 and the extended component of O IIIB-1 is probably density-bounded nebulae. In the case of the density-bounded nebulae, high-ionization photons can escape from the center of the galaxy, and the O<sup>+</sup> region producing the [O II] emission line is small because of the small H I cloud. The density-bounded region at the center might lead to a harder emitted spectrum that ionizes the more extended nebulae. Further observations are needed to confirm whether the physical conditions of the [O III] blobs are really consistent with the density-bounded nebulae.

The authors are very grateful to an anonymous referee for valuable comments that helped improve the article. This work is supported by Faculty of Science, Mahidol University, Thailand, and the Thailand Research Fund (TRF) through a research grant for new scholars (MRG6180279). We thank Moire Prescott for her useful comments. S.Y. thanks David J. Ruffolo for support as a mentor of the TRF research grant. M. O. is supported by the World Premier International Research Center Initiative (WPI Initiative), MEXT, Japan, and KAKENHI (15H02064, 17H01110, and 17H01114) Grant-in-Aid for Scientific Research (A) through the Japan Society for the Promotion of Science.

### Appendix Correction for Dust Attenuation

In order to obtain accurate results of the observed fluxes and the line ratios, we need to take dust extinction into account. For O IIIB-1 and O IIIB-2, we are able to detect the  $H\gamma$  emission

Table 4 Color Excesses of Four [O III] Blobs at z=0.63–0.83 Derived from the Balmer Decrement and SED Fitting Method

[O III] Blobs	E(B -	V) <sub>nebular</sub>	$E(B-V)_{\text{stellar}}$
-	$H\gamma/H\beta$	$H\alpha/H\beta$	SED Fitting
O IIIB-1	$0.33 \pm 0.19$	$0.24 \pm 0.10$	$0.18^{+0.34}_{-0.04}$
O IIIB-2	$0.41\pm0.42$		$0.20^{+0.40}_{-0.20}$
O IIIB-3			$0.34^{+0.36}_{-0.20}$
O IIIB-4			$0.18^{+0.28}_{-0.10}$

lines and use the Balmer decrement to derive the dust attenuation. In addition, we can also detect the  ${\rm H}\alpha$  emission line of O IIIB-1 from the Keck/MOSFIRE spectrum. The observed H $\gamma$ , H $\beta$ , and H $\alpha$  fluxes of O IIIB-1 are  $4.92\times 10^{-17}\,{\rm erg\,s^{-1}\,cm^{-2}}$ ,  $1.24\times 10^{-16}\,{\rm erg\,s^{-1}\,cm^{-2}}$ , and  $4.76\times 10^{-16}\,{\rm erg\,s^{-1}\,cm^{-2}}$ , respectively. These result in H $\gamma$ /H $\beta$  and H $\alpha$ /H $\beta$  line ratios of  $0.40\pm 0.08$  and  $3.84\pm 0.40$ , respectively. The H $\gamma$ /H $\beta$  line ratio for O IIIB-2 is  $0.39\pm 0.26$  because the H $\gamma$  and H $\beta$  emission lines show observed fluxes of  $1.04\times 10^{-16}\,{\rm erg\,s^{-1}\,cm^{-2}}$  and  $2.70\times 10^{-16}\,{\rm erg\,s^{-1}\,cm^{-2}}$ , respectively. The color excess E(B-V) can be derived from the H $\gamma$ /H $\beta$  ratio as follows:

$$E(B - V) = \frac{E(H\beta - H\gamma)}{\kappa(H\beta) - \kappa(H\gamma)}$$
 (5)

$$= \frac{-2.5}{\kappa(\mathrm{H}\beta) - \kappa(\mathrm{H}\gamma)} \times \log_{10} \left[ \frac{0.469}{(\mathrm{H}\gamma/\mathrm{H}\beta)_{\mathrm{obs}}} \right]. \tag{6}$$

Likewise, the  ${\rm H}\alpha/{\rm H}\beta$  line ratio is related to the color excess s

$$E(B - V) = \frac{E(H\beta - H\alpha)}{\kappa(H\beta) - \kappa(H\alpha)}$$
(7)

$$= \frac{-2.5}{\kappa(\mathrm{H}\beta) - \kappa(\mathrm{H}\alpha)} \times \log_{10} \left[ \frac{2.86}{(\mathrm{H}\alpha/\mathrm{H}\beta)_{\mathrm{obs}}} \right]. \tag{8}$$

The intrinsic  $H\gamma/H\beta$  and  $H\alpha/H\beta$  ratios are 0.469 and 2.86, respectively. They are obtained by assuming case B recombination with an electron density of  $10^2 \,\mathrm{cm}^{-3}$  and temperature of  $10^4$  K (Osterbrock 1989). The reddening curve  $\kappa(\lambda)$  is derived by adopting the expression in Calzetti et al. (2000). Substituting  $\kappa(H\gamma) = 5.12$ ,  $\kappa(H\beta) = 4.60$ , and  $\kappa(H\alpha) = 3.33$  into the above equations, we obtain color excesses E(B - V) of  $0.33\pm0.19$  mag and  $0.24\pm0.10$  mag for O IIIB-1 as derived by using the  $H\gamma/H\beta$  and  $H\alpha/H\beta$  line ratios, respectively. These are consistent with each other within  $1\sigma$  uncertainty. For O IIIB-1, we adopt E(B - V) = 0.33 to correct for the dust attenuation. Because the H $\gamma$  and H $\beta$  lines are observed simultaneously with the same instrument, they suffer less from different slit correction or flux calibration as compared to the  ${
m H}lpha$  emission line. The color excess of O IIIB-2 estimated from the  $H\gamma/H\beta$  ratio is 0.41  $\pm$  0.42 mag. These nebular color excesses derived from the Balmer decrement are roughly consistent with those of stellar continuum estimated by the SED fitting method (Yuma et al. 2017) after multiplying by a factor of 0.44 described in Calzetti et al. (2000). For O IIIB-3 and O IIIB-4, whose  $H\gamma$  emission lines are not detected, we estimate nebular color excesses from the stellar color excesses obtained by the SED fitting method (Yuma et al. 2017). The color excesses of all four blobs are listed in Table 4. It is noteworthy that we assumed the constant dust extinction across

the [O III] blobs. We checked the  $H\alpha/H\beta$  ratio profile of O IIIB-1 and found that the  $H\alpha/H\beta$  ratios decrease slightly with increasing distance up to 5–6 kpc from the center of O IIIB-1. However, the ratios are still within the line ratio uncertainty of the entire blob.

### ORCID iDs

### References

```
Abazajian, K. N., Adelman-McCarthy, J. K., Agüeros, M. A., et al. 2009,
   ApJS, 182, 543
Aguirre, A., Dow-Hygelund, C., Schaye, J., & Theuns, T. 2008, ApJ, 689, 851
Alexander, D. M., Swinbank, A. M., Smail, I., McDermid, R., & Nesvadba, N. P. H. 2010, MNRAS, 402, 2211
Allen, M. G., Groves, B. A., Dopita, M. A., Sutherland, R. S., & Kewley, L. J.
   2008, ApJS, 178, 20
Amorín, R., Sommariva, V., Castellano, M., et al. 2014, A&A, 568, L8
Amorín, R. O., Pérez-Montero, E., & Vílchez, J. M. 2010, ApJL, 715, L128 Arthur, S. J., Henney, W. J., Mellema, G., de Colle, F., &
   Vázquez-Semadeni, E. 2011, MNRAS, 414, 1747
Baldwin, J. A., Phillips, M. M., & Terlevich, R. 1981, PASP, 93, 5
Bassett, R., Ryan-Weber, E. V., Cooke, J., et al. 2019, MNRAS, 483, 5223
Bell, E. F., McIntosh, D. H., Katz, N., & Weinberg, M. D. 2003, ApJS,
Benson, A. J., Bower, R. G., Frenk, C. S., et al. 2003, ApJ, 599, 38
Bradshaw, E. J., Almaini, O., Hartley, W. G., et al. 2013, MNRAS, 433, 194
Brammer, G. B., van Dokkum, P. G., Illingworth, G. D., et al. 2013, ApJL,
   765, L2
Bruzual, G., & Charlot, S. 2003, MNRAS, 344, 1000
Calzetti, D., Armus, L., Bohlin, R. C., et al. 2000, ApJ, 533, 682
Cardamone, C., Schawinski, K., Sarzi, M., et al. 2009, MNRAS, 399, 1191
Cheung, E., Bundy, K., Cappellari, M., et al. 2016, Natur, 533, 504
Cicone, C., Maiolino, R., Sturm, E., et al. 2014, A&A, 562, A21
Coil, A. L., Weiner, B. J., Holz, D. E., et al. 2011, ApJ, 743, 46
Dopita, M. A., & Sutherland, R. S. 1996, ApJS, 102, 161
Elbaz, D., Daddi, E., Le Borgne, D., et al. 2007, A&A, 468, 33
Erb, D. K., Quider, A. M., Henry, A. L., & Martin, C. L. 2012, ApJ, 759, 26
Förster Schreiber, N. M., Genzel, R., Bouché, N., et al. 2009, ApJ, 706, 1364
Förster Schreiber, N. M., Genzel, R., Newman, S. F., et al. 2014, ApJ, 787, 38
Fotopoulou, S., Buchner, J., Georgantopoulos, I., et al. 2016, A&A, 587, A142
Fumagalli, M., O'Meara, J. M., & Prochaska, J. X. 2011, Sci, 334, 1245
Genzel, R., Newman, S., Jones, T., et al. 2011, ApJ, 733, 101
Harikane, Y., Ouchi, M., Yuma, S., et al. 2014, ApJ, 794, 129
Heckman, T. M., Armus, L., & Miley, G. K. 1990, ApJS, 74, 833
Heckman, T. M., Lehnert, M. D., Strickland, D. K., & Armus, L. 2000, ApJS,
   129, 493
Ichikawa, K., Ueda, J., Bae, H.-J., et al. 2019, ApJ, 870, 65
Izotov, Y. I., Thuan, T. X., & Guseva, N. G. 2017, MNRAS, 471, 548
Izotov, Y. I., Thuan, T. X., & Privon, G. 2012, MNRAS, 427, 1229
Jansen, F., Lumb, D., Altieri, B., et al. 2001, A&A, 365, L1
Jaskot, A. E., & Oey, M. S. 2013, ApJ, 766, 91
Kashikawa, N., Aoki, K., Asai, R., et al. 2002, PASJ, 54, 819
Kauffmann, G., Heckman, T. M., Tremonti, C., et al. 2003, MNRAS,
   346, 1055
Kewley, L. J., & Dopita, M. A. 2002, ApJS, 142, 35
Kewley, L. J., Dopita, M. A., Sutherland, R. S., Heisler, C. A., & Trevena, J.
   2001, ApJ, 556, 121
Kewley, L. J., Groves, B., Kauffmann, G., & Heckman, T. 2006, MNRAS,
Kornei, K. A., Shapley, A. E., Martin, C. L., et al. 2012, ApJ, 758, 135
```

```
Lamareille, F. 2010, A&A, 509, A53
Lilly, S. J., Carollo, C. M., Pipino, A., Renzini, A., & Peng, Y. 2013, ApJ,
   772, 119
Lilly, S. J., Carollo, C. M., & Stockton, A. N. 2003, ApJ, 597, 730
Lin, L., Lin, J.-H., Hsu, C.-H., et al. 2017, ApJ, 837, 32
Liu, G., Zakamska, N. L., Greene, J. E., Nesvadba, N. P. H., & Liu, X. 2013,
   MNRAS, 430, 2327
Mannucci, F., Cresci, G., Maiolino, R., Marconi, A., & Gnerucci, A. 2010,
   MNRAS, 408, 2115
Martin, C. L. 2005, ApJ, 621, 227
Martin, C. L., Shapley, A. E., Coil, A. L., et al. 2012, ApJ, 760, 127
McLean, I. S., Steidel, C. C., Epps, H. W., et al. 2012, Proc. SPIE, 8446,
Mutch, S. J., Croton, D. J., & Poole, G. B. 2013, MNRAS, 435, 2445
Nakajima, K., & Ouchi, M. 2014, MNRAS, 442, 900
Nakajima, K., Ouchi, M., Shimasaku, K., et al. 2013, ApJ, 769, 3
Nesvadba, N. P. H., Lehnert, M. D., De Breuck, C., Gilbert, A. M., &
   van Breugel, W. 2008, A&A, 491, 407
Newman, S. F., Genzel, R., Förster-Schreiber, N. M., et al. 2012a, ApJ, 761, 43
Newman, S. F., Shapiro Griffin, K., Genzel, R., et al. 2012b, ApJ, 752, 111
Noeske, K. G., Weiner, B. J., Faber, S. M., et al. 2007, ApJL, 660, L43
Oey, M. S., & Kennicutt, R. C., Jr. 1997, MNRAS, 291, 827
Oke, J. B., & Gunn, J. E. 1983, ApJ, 266, 713
Oppenheimer, B. D., Davé, R., Kereš, D., et al. 2010, MNRAS, 406, 2325
Osterbrock, D. E. 1989, S&T, 78, 491
Pagel, B. E. J., Edmunds, M. G., Blackwell, D. E., Chun, M. S., & Smith, G.
   1979, MNRAS, 189, 95
Pellegrini, E. W., Oey, M. S., Winkler, P. F., et al. 2012, ApJ, 755, 40
Prochaska, J. X., Kasen, D., & Rubin, K. 2011, ApJ, 734, 24
Ranalli, P., Koulouridis, E., Georgantopoulos, I., et al. 2016, A&A, 590, A80
Rubin, K. H. R., Prochaska, J. X., Koo, D. C., et al. 2014, ApJ, 794, 156
Rupke, D. S., Veilleux, S., & Sanders, D. B. 2005a, ApJS, 160, 87
Rupke, D. S., Veilleux, S., & Sanders, D. B. 2005b, ApJS, 160, 115
Rupke, D. S. N., Gültekin, K., & Veilleux, S. 2017, ApJ, 850, 40
Salpeter, E. E. 1955, ApJ, 121, 161
Schawinski, K., Koss, M., Berney, S., & Sartori, L. F. 2015, MNRAS,
  451, 2517
Schirmer, M., Diaz, R., Holhjem, K., Levenson, N. A., & Winge, C. 2013, ApJ,
Schirmer, M., Malhotra, S., Levenson, N. A., et al. 2016, MNRAS, 463, 1554
Shields, G. A. 1990, ARA&A, 28, 525
Shirazi, M., & Brinchmann, J. 2012, MNRAS, 421, 1043
Shirazi, M., Brinchmann, J., & Rahmati, A. 2014, ApJ, 787, 120
Silk, J., & Rees, M. J. 1998, A&A, 331, L1
Simpson, C., Martínez-Sansigre, A., Rawlings, S., et al. 2006, MNRAS,
   372, 741
Simpson, C., Rawlings, S., Ivison, R., et al. 2012, MNRAS, 421, 3060
Somerville, R. S., Hopkins, P. F., Cox, T. J., Robertson, B. E., & Hernquist, L.
   2008, MNRAS, 391, 481
Soto, K. T., Martin, C. L., Prescott, M. K. M., & Armus, L. 2012, ApJ, 757, 86
Steidel, C. C., Erb, D. K., Shapley, A. E., et al. 2010, ApJ, 717, 289
Strüder, L., Briel, U., Dennerl, K., et al. 2001, A&A, 365, L18
Sun, A.-L., Greene, J. E., & Zakamska, N. L. 2017, ApJ, 835, 222
Thuan, T. X., & Izotov, Y. I. 2005, ApJS, 161, 240
Tremonti, C. A., Heckman, T. M., Kauffmann, G., et al. 2004, ApJ, 613, 898
Turner, M. J. L., Abbey, A., Arnaud, M., et al. 2001, A&A, 365, L27
Ueda, Y., Watson, M. G., Stewart, I. M., et al. 2008, ApJS, 179, 124
Ulrich, M.-H., Maraschi, L., & Urry, C. M. 1997, ARA&A, 35, 445
van de Voort, F., Schaye, J., Booth, C. M., & Dalla Vecchia, C. 2011,
      JRAS, 415, 2782
Veilleux, S., & Osterbrock, D. E. 1987, ApJS, 63, 295
Weber, J. A., Pauldrach, A. W. A., & Hoffmann, T. L. 2019, A&A, 622, A115
Weiner, B. J., Coil, A. L., Prochaska, J. X., et al. 2009, ApJ, 692, 187
Yabe, K., Ohta, K., Iwata, I., et al. 2009, ApJ, 693, 507
Yang, H., Malhotra, S., Rhoads, J. E., & Wang, J. 2017, ApJ, 847, 38
Yuma, S., Ouchi, M., Drake, A. B., et al. 2013, ApJ, 779, 53
Yuma, S., Ouchi, M., Drake, A. B., et al. 2017, ApJ, 841, 93
Zhang, K., Yan, R., Bundy, K., et al. 2017, MNRAS, 466, 3217
```